Chapter III Tomographic Imaging of 3-D Seismic Velocity Structure beneath the Central and East Java Region, Indonesia

III.1 Data and Model Parameterization

We used P- and S-arrivals determined by Muttaqy et al. (2021 - in review) that were manually re-picked from waveforms recorded at 27 stations of the Meteorological, Climatological, Geophysical Agency of Indonesia (BMKG) for earthquakes within the time period of January 2009 to September 2017 using Seisgram2K (Lomax and Michelini, 2009). The earthquake locations were then determined using the NLLoc program (Lomax et al., 2000) with the global velocity model of AK135 (Kennett et al., 1995) for the longitude and latitude ranges of 108º-118ºE and 5º-12ºS, respectively, with at least six high-quality phase picks and magnitude (Mw) >3. Most of the earthquakes are distributed in the south of the island, which results in a maximum azimuthal gap of greater than 180º with the average hypocenter location errors are 5.6, 15.5 and 20.5 km in the x, y, and z directions, respectively. In total, there are 1,488 initial events with 11,192 P- and 11,192 S-phases which were used for the tomographic inversion (Figure III.1a and B.1 in Appendix B). The estimated picking errors for the observed P- and S-arrivals are 0.1886 s and 0.297 s, respectively. This results in better locations compared to the BMKG catalog, which uses Geiger method (Geiger, 1912) with the global velocity model IASP91. The BMKG location, which use a fewer number of S-arrivals for quick determination have a fixed-depths of 10 km for the shallow earthquakes and larger residual times. A detailed description of the seismicity analysis for the events has been provided in Muttaqy et al. (2021 - in review).

The choice of a particular model parameterization is always essential for assessing the quality of the 3-D tomographic images, considering the recovery of checkerboard resolution tests (CRT) over various grid size models. Several factors need to be considered, such as the size of features that can be resolved, distribution of available events and stations, and the computing limitations (Kissling et al., 2001). In this study, we used a 50x50 km^2 grid spacing horizontally and various grid spacings of 10-100 km in the vertical direction (Figure III.1b). Table III.1 shows the exact size of grid spacing horizontally and vertically. The initial velocity model used in this study was the 1-D seismic velocity model of Central Java (Koulakov et al., 2007) with a constant Vp/Vs ratio of 1.75, based on the plotted Wadati diagram of this study (Figure B.1 in Appendix B).

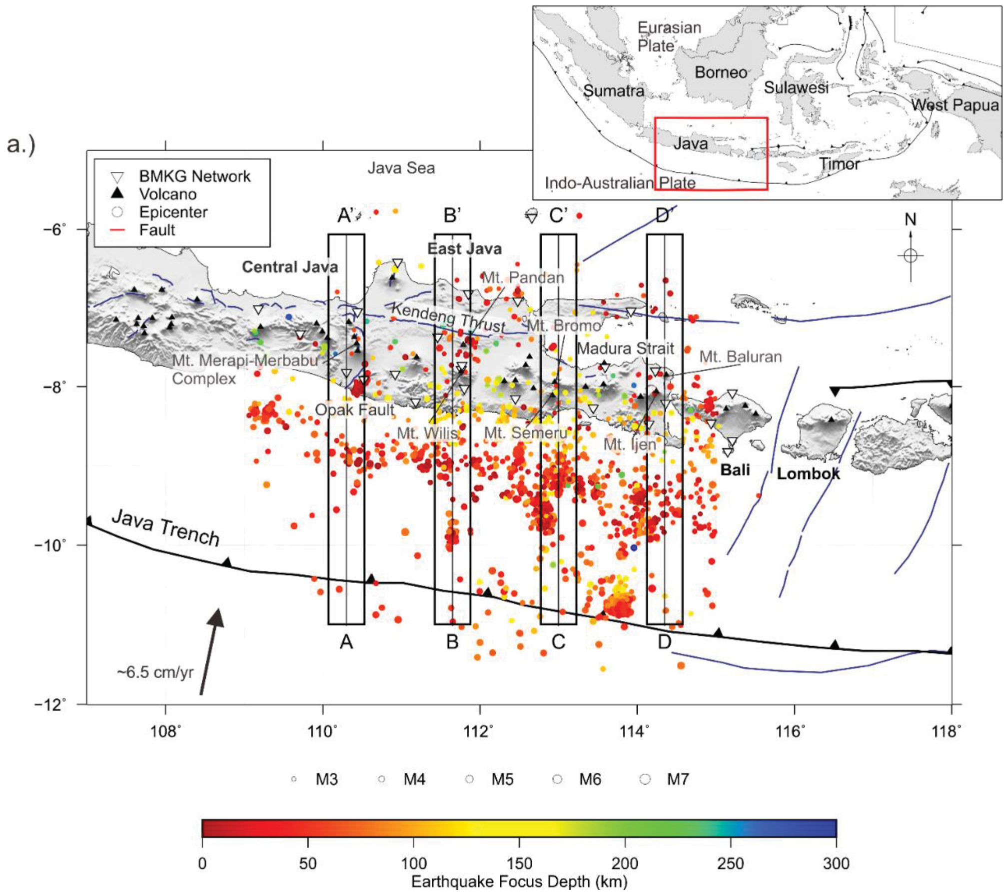

Figure III.1 (a) Map showing the distribution of 27 BMKG stations (inverted triangles) and seismicity used in this study from January 2009 to September 2017. The rectangles A-D are the area used to plot the vertical cross-section in Figure III.7 and III.9 (b) Grid node parameterization used for the seismic tomographic inversion (plus signs). The colors of the circles represent earthquake focus depth, active fault lineaments (blue lines) and volcanoes (black triangles) (Marliyani, 2016; Pusat Studi Gempa Nasional (PuSGeN), 2017).

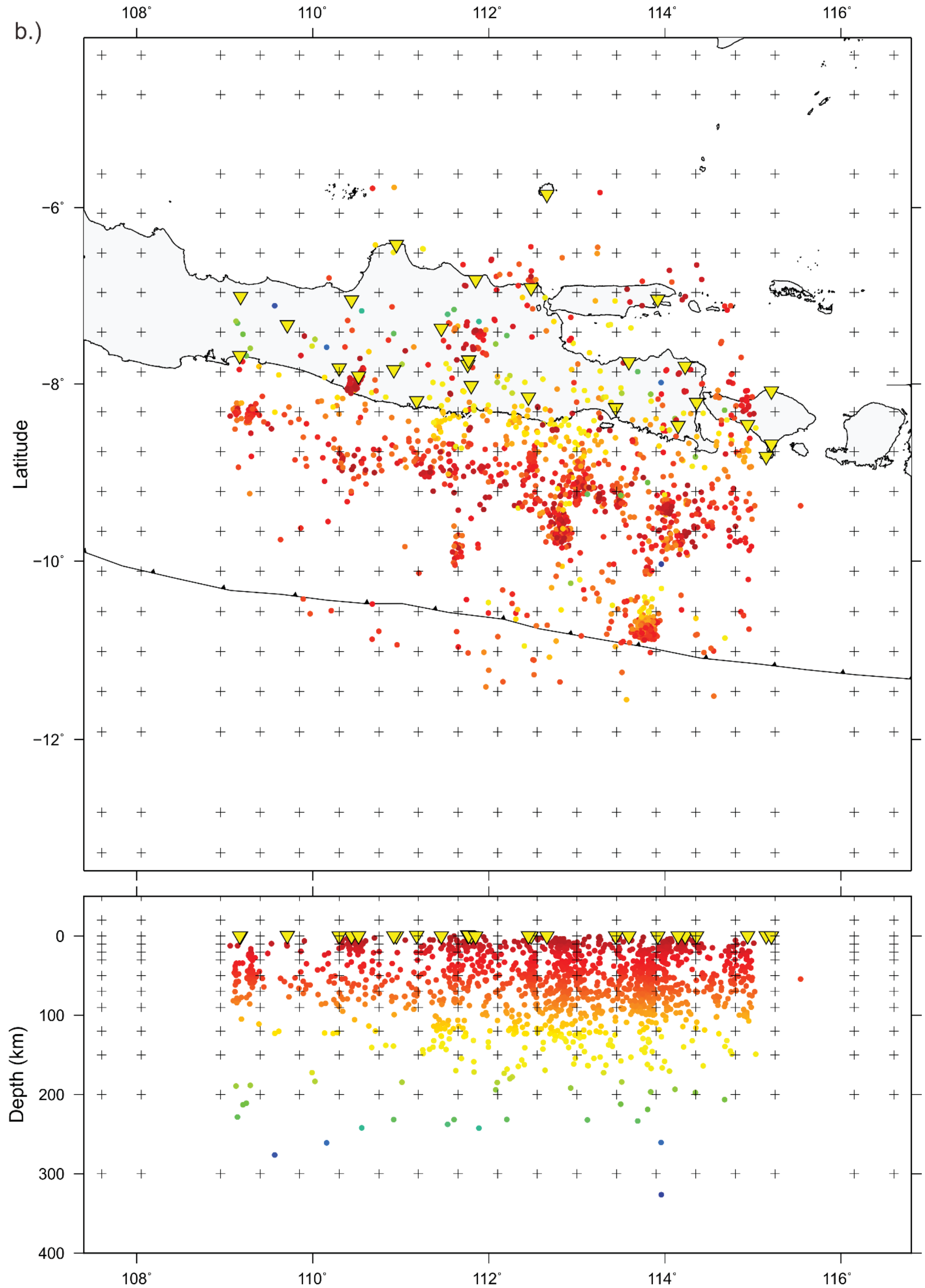

Figure III.1 continued

III.2 Ray Tracing

The ray paths were determined by using the pseudo bending technique of Um and Thurber (1987). This technique is based on Fermat's principle, where the seismic wave propagates along the ray path with the minimum travel time. Thus, the ray equations can be written as:

$$-\frac{\boldsymbol{d^2r}}{\boldsymbol{ds^2}} = \frac{\left[(\boldsymbol{grad\,V}) - \frac{\boldsymbol{dv}}{\boldsymbol{ds}} \cdot \frac{\boldsymbol{d\vec{r}}}{\boldsymbol{ds}}\right]}{\boldsymbol{V}} \qquad \text{(III.1)}$$

where $\vec{r}$ is the position vector along the ray, and s is the parameter of path length, and v is the seismic velocity. The right side of equation (III.1) is simply the component of the velocity gradient parallel to the ray path. Thus, equation III.1 states that the component of the velocity gradient normal to the ray vector is always antiparallel to the ray path curvature (Zhao, 2015). The illustration of the pseudo-bending method is shown in Figure III.2.

Table III.1 Grid node parameterization used in this study.

Grid direction	Grid interval distance from a central node (km)
X	-500.0 -450.0 -350.0 -300.0 -250.0 -200.0 -150.0 -100.0 -50.0 0.0 50.0 100.0 150.0 200.0 250.0 300.0 350.0 450.0 500.0
Y	-500.0 -450.0 -350.0 -300.0 -250.0 -200.0 -150.0 -100.0 -50.0 0.0 50.0 100.0 150.0 200.0 250.0 300.0 350.0 450.0 500.0
Z	-50.0 -20.0 0.0 10.0 20.0 30.0 50.0 70.0 90.0 120.0 150.0 200.0 300.0 500.0 700.0

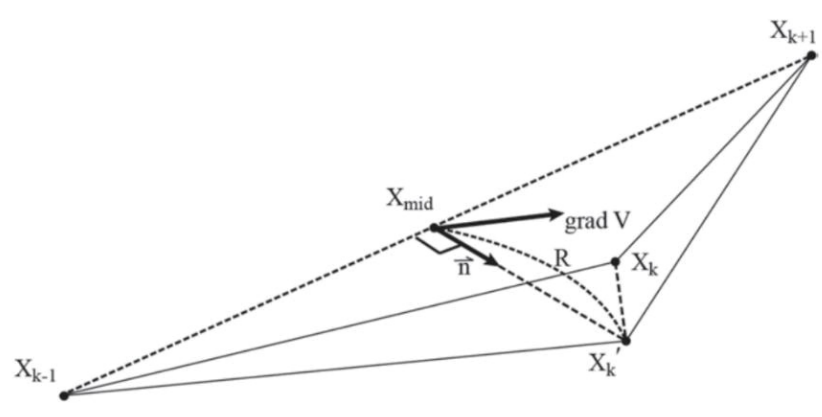

Figure III.2 Illustration of the three-point perturbation scheme in pseudo ending method (Um and Thurber, 1987).

Consider three adjacent points of X_{k-1}, X_{mid}, dan X_{k+1} defining the path. When there is no velocity variation both vertically and horizontally between X_{k-1} dan X_{k+1}, the ray will propagate directly through X_{mid} as a straight line. If there's velocity discontinuity between X_{k-1} dan X_{k+1}, then the ray path will be bent to the X_k point. A new point $X_{k'}$ instead of the previous point X_k is sought to minimize the travel time along the segment. Two variables to be computed are the direction $\vec{n}$ and the amount R of offset from the mid-point X_{mid}.

The distribution of ray paths is shown in Figure III.3 with the station locations and grid node distribution used in this study. Based on the ray paths distribution, we can quickly analyze which region has a good resolution or unresolved due to a lack of ray paths. Figure III.3 indicates that our tomographic inversion will resolve better south of the island. It is good enough to provide information about the three-dimensional distribution of seismic velocities of the Java subduction zone.

III.3 Tomographic Inversion

For the local tomographic inversion, we applied the SIMULPS12 code (Evans et al., 1994), which performs an iterative damped least-squares inversion method to calculate both hypocenter relocation and velocity structure, simultaneously. P-arrival times and S-P times are inverted directly for Vp and Vp/Vs ratio. It is more reliable to invert for Vp and Vp/Vs than Vp and Vs separately when there are fewer high-quality S-arrivals (Eberhart-Phillips, 1986). The procedure starts from determining the calculated arrival times using trial hypocenters, origin times, an initial model of the seismic velocity structure, and the pseudo-bending technique of Um and Thurber (1987) for the ray tracing (Figure III.3). The residuals between observed and calculated arrival times can be related to perturbations to the velocity structure parameters that are iteratively performed in order to minimize the weighted root-mean-square (RMS) misfit.

In a tomographic inversion, damping regularization is always required for obtaining a reliable inversion result. Because, in practice, the distribution of seismic stations and earthquakes available in a study area is usually not uniform, leading to a very heterogeneous distribution of ray paths. There are the grid nodes that well-sampled by the rays, whereas certain nodes are poorly sampled. If the damping regularization is avoided, the solution at the poorly sampled nodes will become unacceptably large, and the tomographic image would become a mess. The appropriate damping parameter is needed to prevent such a situation. It depends on the uniformity of the ray distribution (Zhao, 2015).

During the inversion, there are the grid nodes that were both well-sampled and poorly sampled by the rays. Because, in practice, the distribution of seismic stations and earthquakes available in a study area is usually not uniform, leading to a very heterogeneous distribution of ray paths. Hence, damping regularization is required to stabilize the solution which is determined by comparing data variance with model variance, as shown in the trade-off curves of Figure III.4 for a series of one-step inversions within a range of damping values (Eberhart-Phillips, 1986). If the damping regularization is avoided, the solution at the poorly sampled nodes will become unacceptably large, and the tomographic image would become a mess. The appropriate damping parameter is needed to prevent such a situation. It depends on the uniformity of the ray distribution (Zhao, 2015).

An appropriate damping value of 50 that balances the data and model variance was selected for both Vp and Vp/Vs (Figure III.4). The earthquakes are relocated at each iteration step using the current determined 3-D velocity model. We used a weighting scheme as a function of residual with the full weight (1.0) for residuals less than 0.15 s, zero-weight (0.0) for residuals greater than 10 s, and an intermediate value of 0.02 for residuals near 1.5 s. The linear tapers are from 0.15 to 1.5 s and 1.5 to 10 s, so that the high residual data above 10 s will be automatically discarded in early inversion steps. We set the maximum number of iterations up to 20. However, the inversion automatically stopped at the 15th iteration when the convergence and least weighted RMS were achieved (Figure III.5). An F-test in SIMULPS is used to provide a stopping criterion, indicating that variance reduction has become insignificant with further iterations.

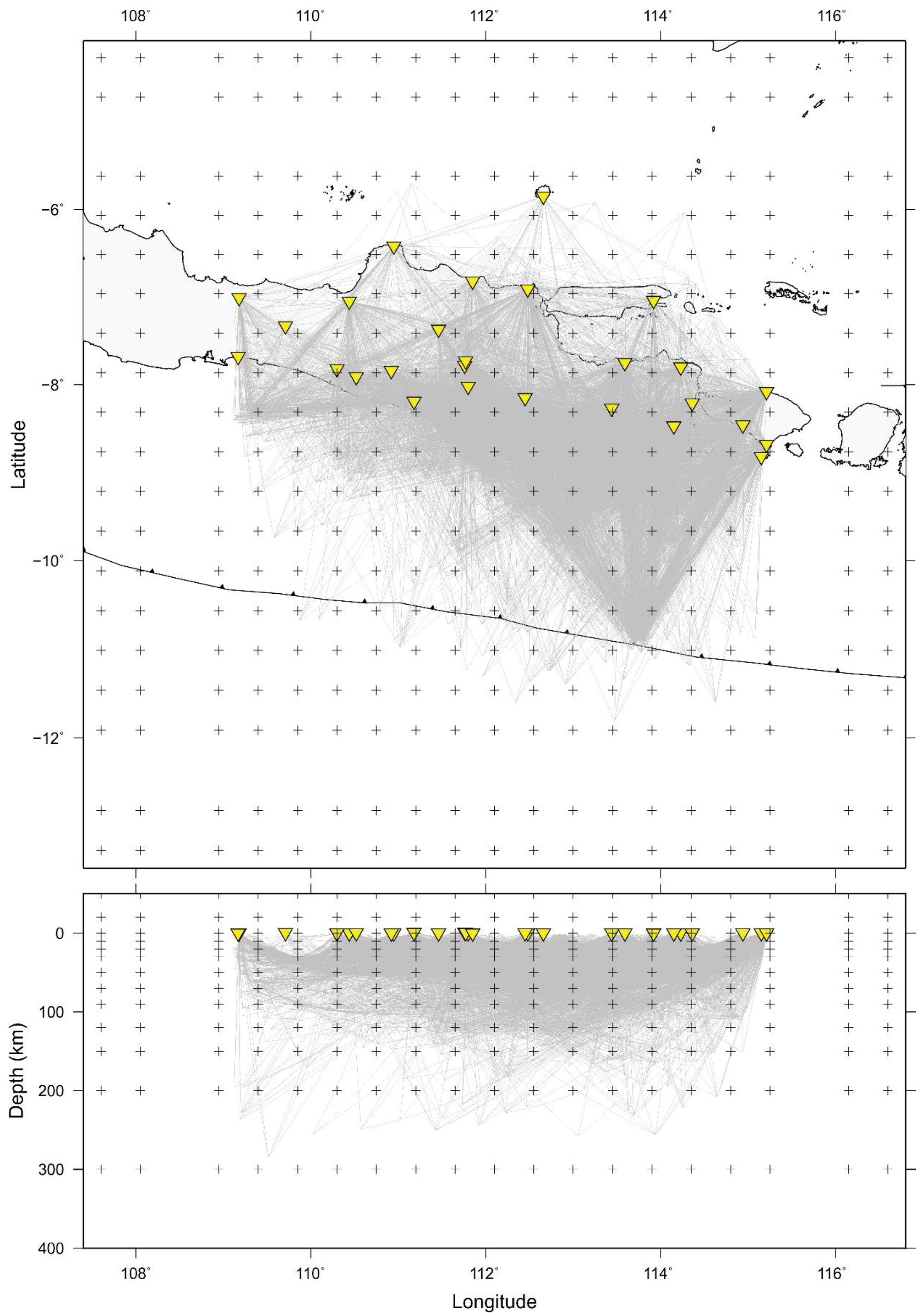

Figure III.3 Grid node parameterization used for the seismic tomography inversion (plus signs) and ray path distribution (gray lines) that connect the hypocenters to the stations (yellow inverted triangles) through the 3-D seismic velocity model of our results.

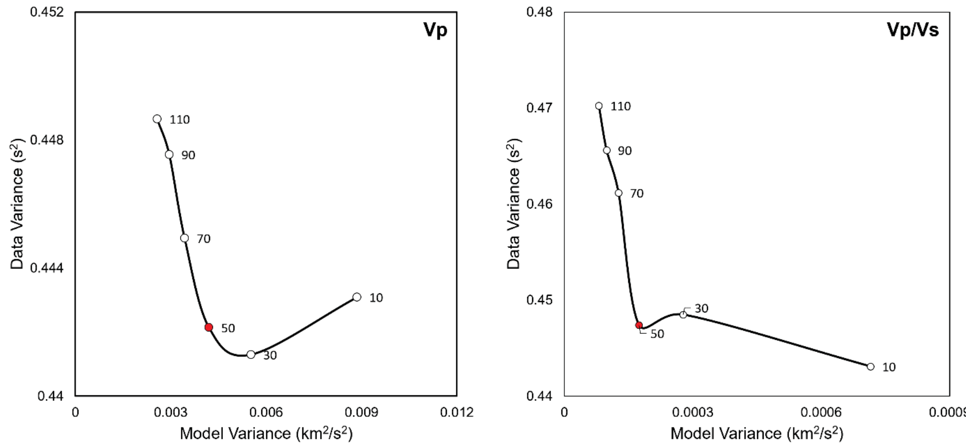

Figure III.4 Trade-off curves showing model variance versus data variance for selecting optimal damping values in the inversions. Damping value of 50 (red dots) was selected for both Vp and Vp/Vs inversions.

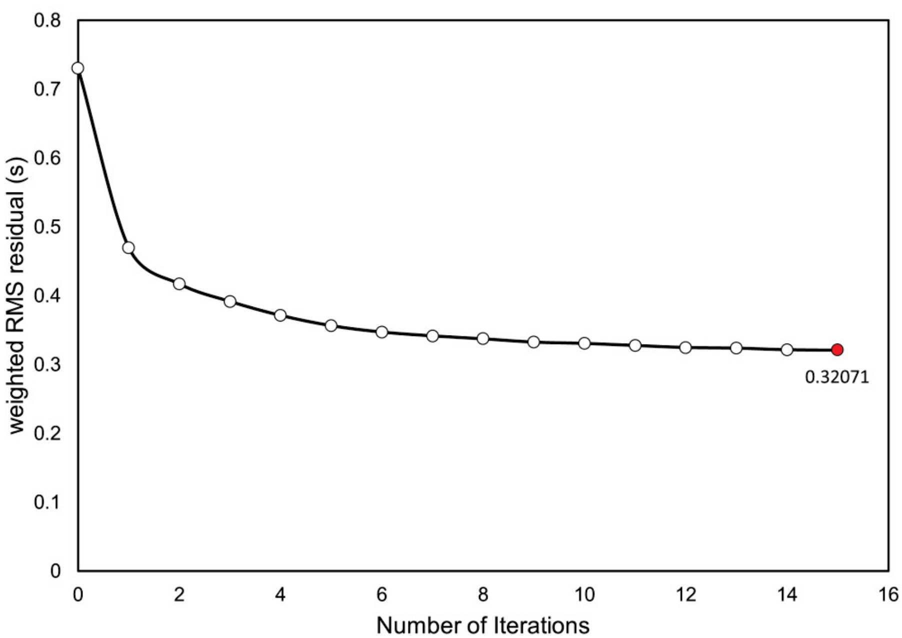

Figure III.5 Graph showing the weighted RMS residual time of model for each iteration. The inversion reached the convergence at the 15^{th} iteration with the value of 0.32071 s.

III.4 Resolution Tests

The resolution test is required to estimate which area of the tomogram has a better resolution, and it is reliable to do the interpretation. The capability of the parameterized model and the distribution of data to resolve the structure beneath the study area can be tested with synthetic data constructed using the same earthquake and station locations as in our data set. We used several resolution tests, i.e., Checkerboard Resolution Test (CRT) (Leveque et al., 1993), Derivative Weighted Sum (DWS) (Toomey and Foulger, 1989), and Diagonal Resolution Element Matrix (DREM) (Menke, 1989).

Checkerboard resolution test (CRT) is the most common way to examine the resolution of seismic tomography. For adjacent grid nodes of the model, we perturbed the velocity by ± 10% relative to the initial 1-D velocity model and then calculated the travel times to the stations for each earthquake location. This synthetic data set of travel times was then inverted for the velocity structure to examine how well the checkerboard pattern was recovered. The results of this test are shown for Vp and Vp/Vs in Figure III.6 and III.7. In order to evaluate the resolution test more appropriately, we added Gaussian noise with a mean of -0.0401 and a standard deviation of 0.6149 s to synthetic data (Figure C.3 and C.4 in Appendix C). This synthetic data set of travel times was then inverted for the velocity structure using the same number of iterations as the real inversion to examine how well the checkerboard pattern was recovered and is usually consistent with the higher values of DWS, RHC, and DRE.

Derivative Weighted Sum (DWS) provides an average relative measure of the density of seismic rays around a given node. The area with a higher DWS value is usually consistent with the CRT results; it becomes reliable to interpret. Therefore, poorly sampled nodes are indicated by relatively small DWS values. The DWS of nth velocity parameter α_n is defined as (Toomey and Foulger, 1989):

$$\boldsymbol{DWS}_{(\alpha_n)} = \boldsymbol{N}\sum_{i}\sum_{j}\left\{\int_{P_{ij}} \boldsymbol{\omega_n(x)\,ds}\right\} \quad \text{(III.2)}$$

where i and j are the event and station indices, ω is the weight used in the linear interpolation and depends on the coordinate position, P_{ij} is the ray path between i and j, and N is a normalization factor that takes into account the volume influenced by α_n. The DWS value distribution is usually displayed in the logarithmic scale, as shown in Figure C.1 and C.2 in Appendix C.

Diagonal Resolution Element Matrix (DREM) value represents the misfit between predicted and observed value that defined as (Menke, 1989):

$$[\boldsymbol{R}] = [\boldsymbol{M}^{\boldsymbol{T}}\boldsymbol{M} + \boldsymbol{L}]^{-\boldsymbol{1}}[\boldsymbol{M}^{\boldsymbol{T}}\boldsymbol{M}] \tag{III.3}$$

where M are matrices containing partial derivatives of the traveltime with respect to the hypocenter and velocity parameters, and L is a matrix containing damping parameter. The DREM value distribution is usually displayed in the range of 0-1, which defines wheater the model is unresolved or entirely resolved, as shown in Figure C.1 and C.2 in Appendix C.

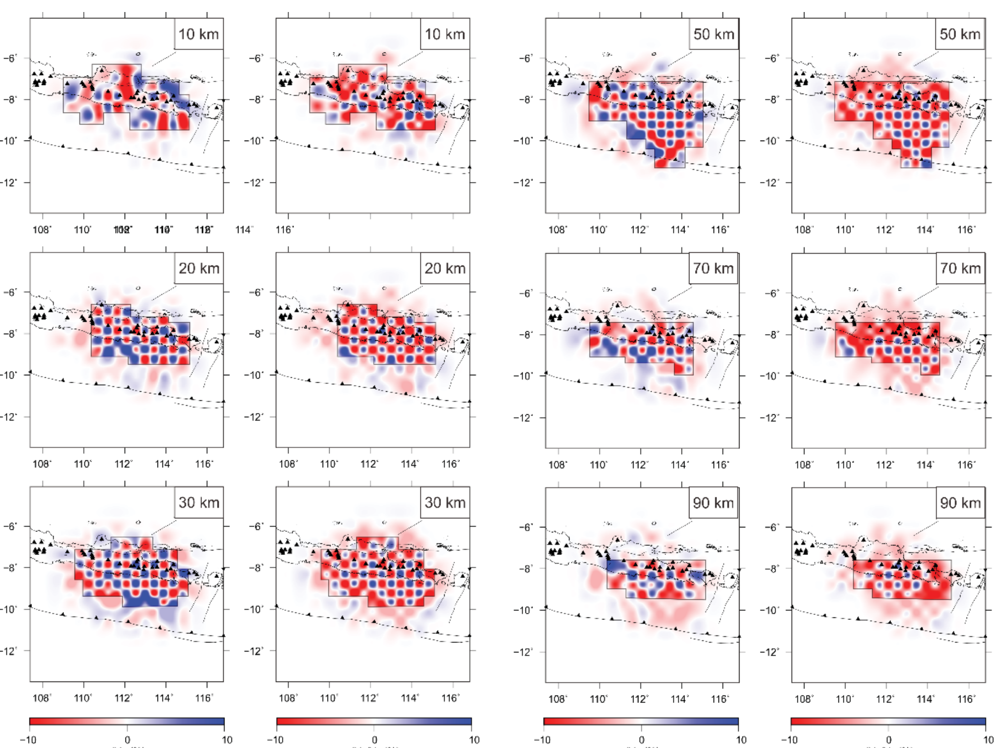

Figure III.6 Results of checkerboard resolution test for Vp and Vp/Vs ratio at depths of 10-90 km beneath the study area. Blue and red colors represent positive and negative perturbations relative to the initial model, respectively. Dashed polygons are the area recovered by this study. Red lines and triangles indicate the fault and volcano distribution, respectively.

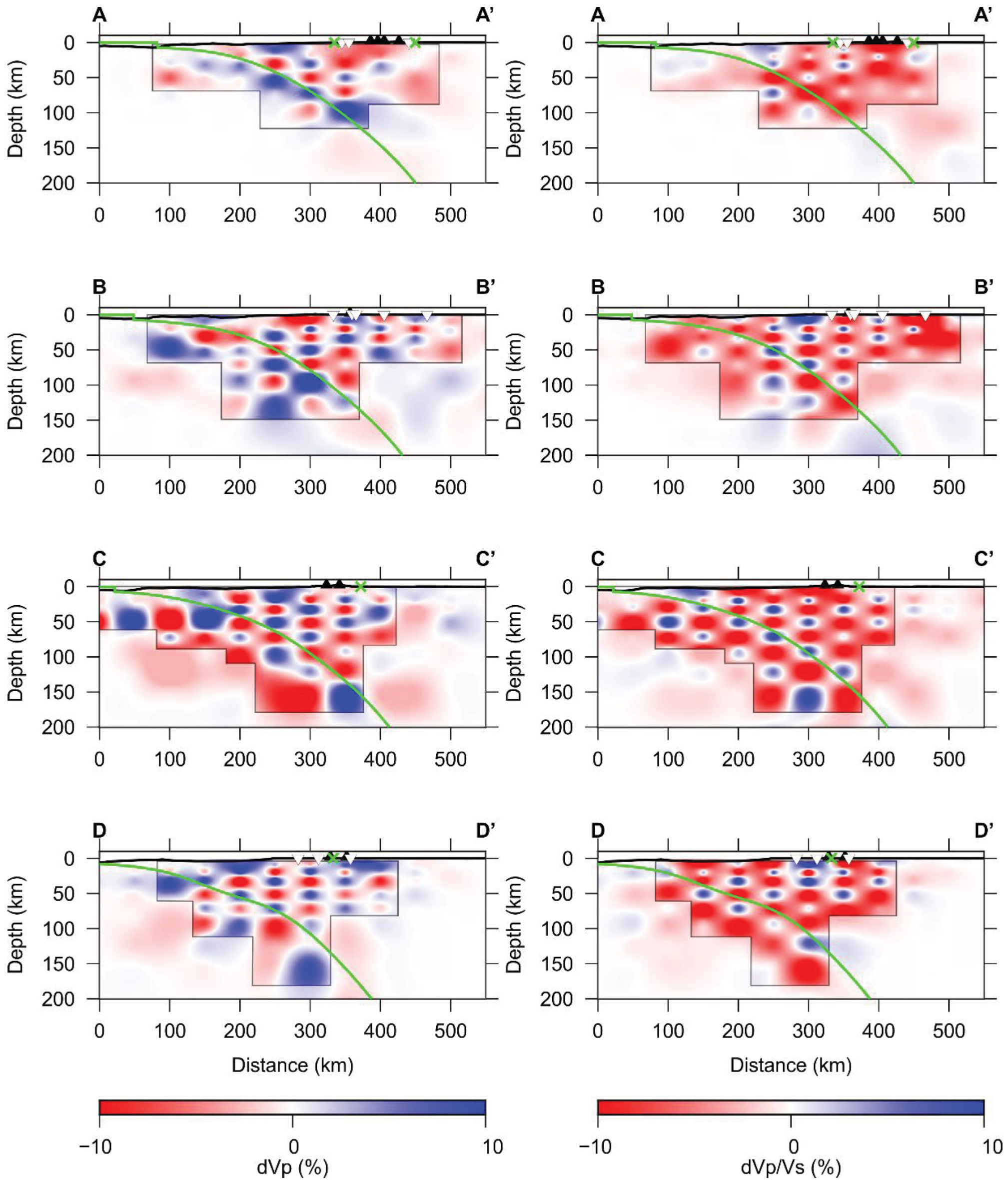

Figure III.7 Results of checkerboard resolution test for Vp and Vp/Vs ratio in vertical direction across Mt. Merapi-Merbabu (A-A'), Mt. Wilis-Pandan (B-B'), Mt. Semeru-Bromo (C-C'), and Mt. Ijen-Baluran (D-D'). Green lines and crosses indicate the slab 2.0 model (Hayes et al., 2018) and faults, respectively. Black triangles show locations of volcanoes.

The CRT results highlight the resolved area within the dashed polygons in Figures III.6 and III.7 for horizontal and vertical sections, respectively, which show a reasonably good resolution for the study area at depths of 10 to 90 km. Following most studies that use the checkerboard test, if the inversion results show that one grid/block has the same anomaly (positive or negative) as the input model, even with a reduction in amplitude due to the implementation of damping, we consider that block to be resolved by the data while considering the limitations of CRT (Rawlinson and Spakman, 2016). The similar areas are consistent with relatively high values for DRE, DWS, and RHC. Fairly high resolution is obtained around the slab model 2.0 (Hayes et al., 2018) and the mantle wedge, since many earthquakes are situated in the plate boundary and many seismic rays travel to the stations onshore, providing a relatively high density of seismic rays around given nodes beneath the region. Below 150 km, the resolution becomes smeared due to the sparse distribution of deep earthquakes.

III.5 Vp, Vs, and Vp/Vs Models

After the 15th iteration, the tomographic inversion was automatically stopped to update the velocity model and relocate the seismicity when the convergence and least weighted RMS had been reached (Figure III.5). It leads to a total weighted RMS reduction from 0.73022 to 0.32071 s with the P- and S-P data variances of 0.1483 and 0.0032 s^2, respectively. Maps of seismicity distribution before and after relocation are shown in Figure B.2 and B.3 in Appendix B, showing that the relocated seismicity distribution is more clustered and statistically improved compared to the initial locations. The RMS residuals are mostly below 0.5 s with an average value of 0.216 s (Figure B.4 in Appendix B). In addition, the travel time residuals associated with the initial and final model are represented as histograms in Figure B.4 in Appendix B, in which most of the value of travel time residuals are in the range of ± 0.75 s.

The final tomographic images of Vp and Vs (Figure III.8 and III.9) are shown as percent perturbations relative to the initial 1-D seismic velocity model of Central Java (I. Koulakov et al., 2007). The blue and red colors represent high and low-velocity changes, respectively. The Vp/Vs values are shown in absolute values (Figure III.8 and III.9). The Vp/Vs ratio is related to Poisson's ratio, a physical property of elastic materials. Distributions of Vp/Vs values indirectly correspond to the variations of pressure, presence of fluid, strength, and temperature

(Christensen, 1996; Jo and Hong, 2013; Lin et al., 2016). For this reason, the Vp/Vs ratio has been widely used to infer structural properties of subducting slabs such as the presence of partial melts or fluid-saturated medium (e.g. Nakajima et al. 2001; Zhang et al. 2004; Eberhart-Phillips et al. 2005; Nugraha and Mori 2006; Reyners et al. 2006; Koulakov et al. 2007; Tsuji et al. 2008; Rohadi et al. 2013; Rosalia et al. 2019). Based on the results of the resolution tests (Figure III.6 and III.7, Appendix C), the regions where the results are considered well constrained are within the dashed polygons.

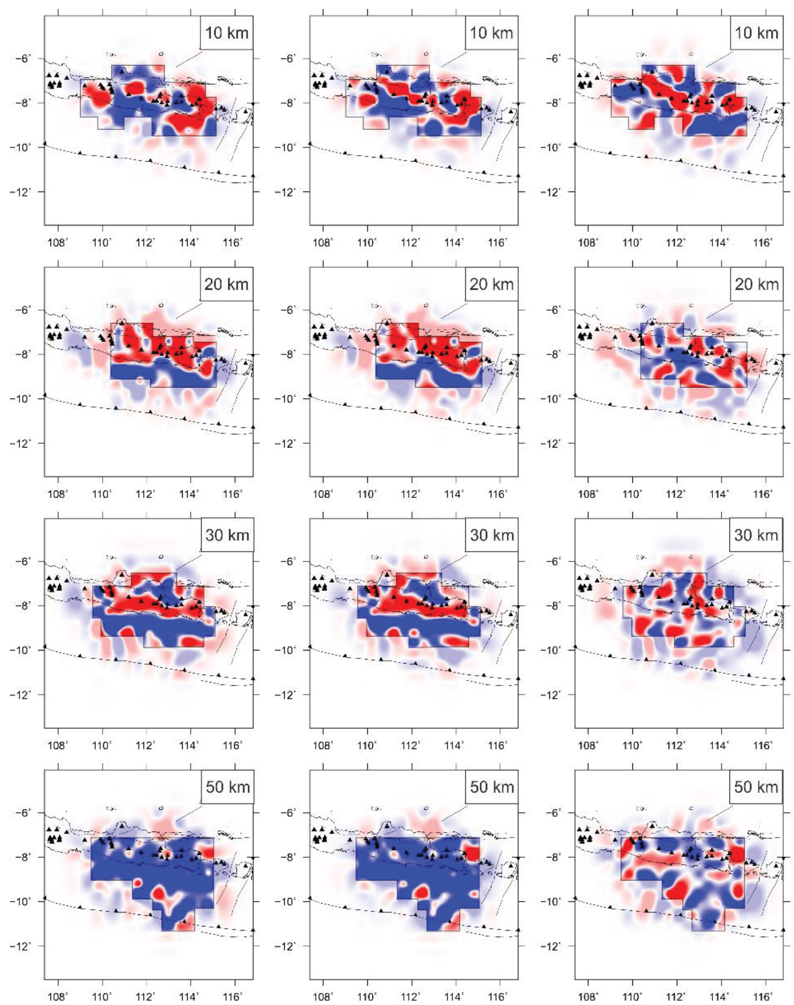

Figure III.8 Horizontal sections for Vp, Vs, and Vp/Vs ratio resulting from tomographic inversions at depths 10-90 km. Dashed polygons are the areas with reliable velocity structure results in this study. Red lines and triangles indicate the faults and volcanoes, respectively.

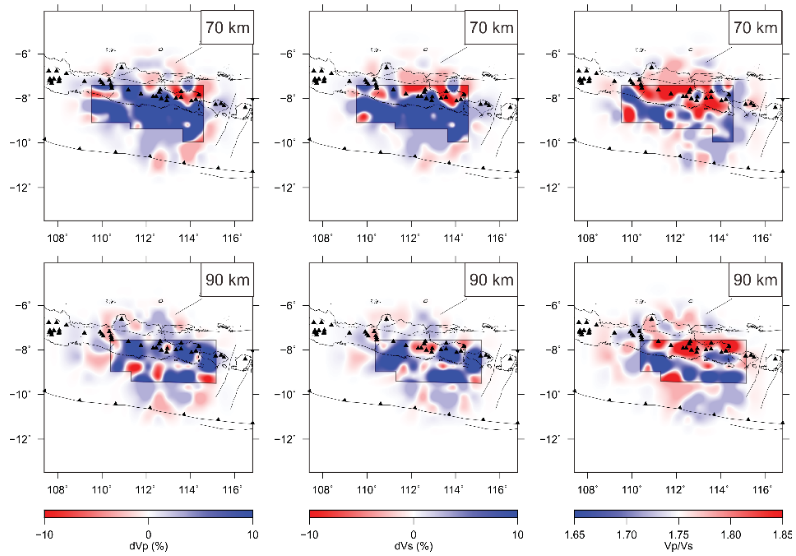

Figure III.8 continued

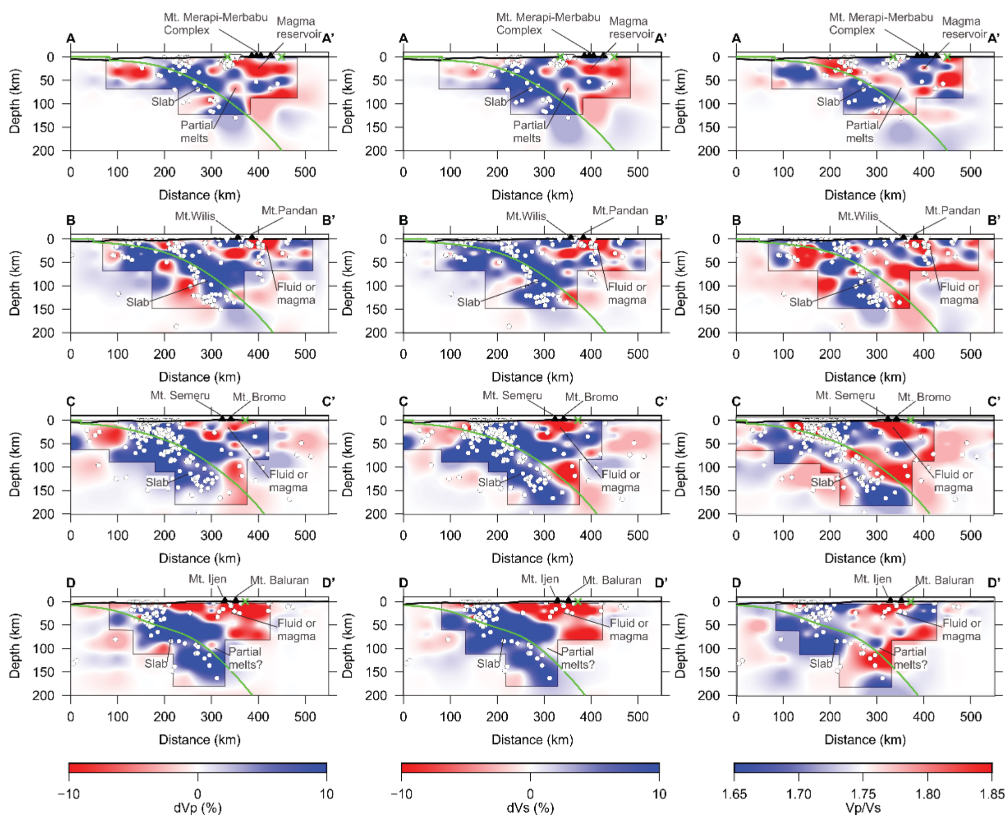

Figure III.9 Vertical sections for Vp, Vs and Vp/Vs ratio with relocated seismicity across Mt. Merapi-Merbabu (A-A'), Mt. Wilis-Pandan (B-B'), Mt. Semeru-Bromo (C-C'), and Mt. Ijen-Baluran (D-D'). Green lines and crosses indicate the slab 2.0 model (Hayes et al., 2018) and faults, respectively. Black triangles show locations of volcanoes.

The horizontal sections of the tomographic results are shown from the depth of 10 km to 90 km (Figure III.8). The map of Bouguer gravity anomaly in Figure III.10a shows correlated features, which is taken from Center for Geological Survey (PSG) (https://geology.esdm.go.id/). In general, we observed that the low velocities (Vp and Vs) dominate around the volcanic complex of the study area which may reflect some features such as sediments or magmatism beneath the volcanoes (Nakajima et al., 2001; Zhao, 2015). These strong low-velocity anomalies can be observed from the depth of 10 km to 30 km beneath Mt. Lawu, Mt. Wilis, and Malang volcanic complex; and from 20 km to 30 km beneath Mt. Merapi-Merbabu complex and Mt. Ijen-Baluran. The estimated Vp/Vs ratio for these regions is also relatively high (> 1.75), suggesting the presence of fluids or partial melts in the sedimentary layer of the Kendeng basin. It correlates with the location of the strong negative Bouguer gravity anomaly of more than -75 mGal, which is at least 400 km long, parallel to the mainland (Figure III.10a) (Smyth et al., 2005, 2008; Waltham et al., 2008) and previous tomographic studies which also confirmed the low-velocity anomaly area beneath Mt. Merapi-Lawu in Central Java with a high Vp/Vs ratio of 1.9 (Koulakov et al., 2007; Rohadi et al., 2013; Wagner et al., 2007; Zulfakriza et al., 2014).

a.)

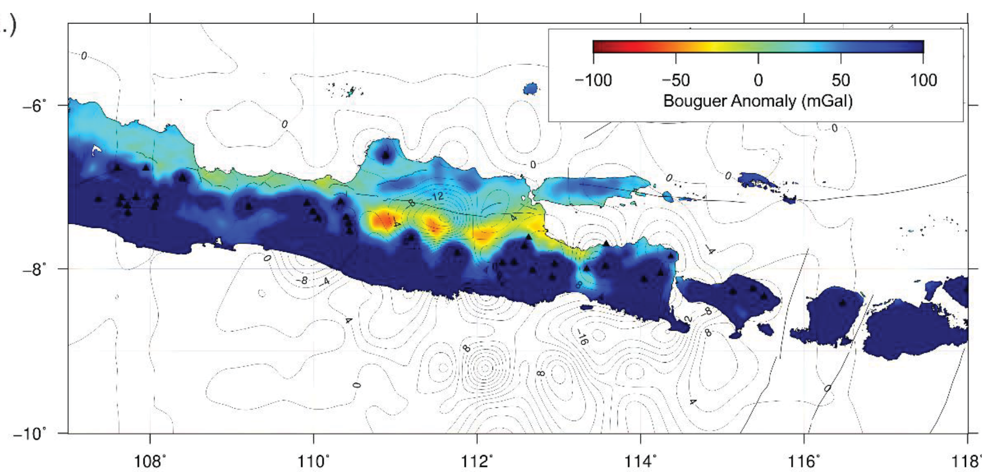

Figure III.10 (a) Map of Bouguer gravity anomaly Center for Geological Survey (PSG) overlayed by Vp perturbation at 10 km depth (black contour) and (b) marine free-air gravity anomaly (Sandwell et al., 2014) in Central and East Java region. Black lines indicate faults and trench delineation. Black triangles are the volcanoes. Inset shows the location of subducted seamount.

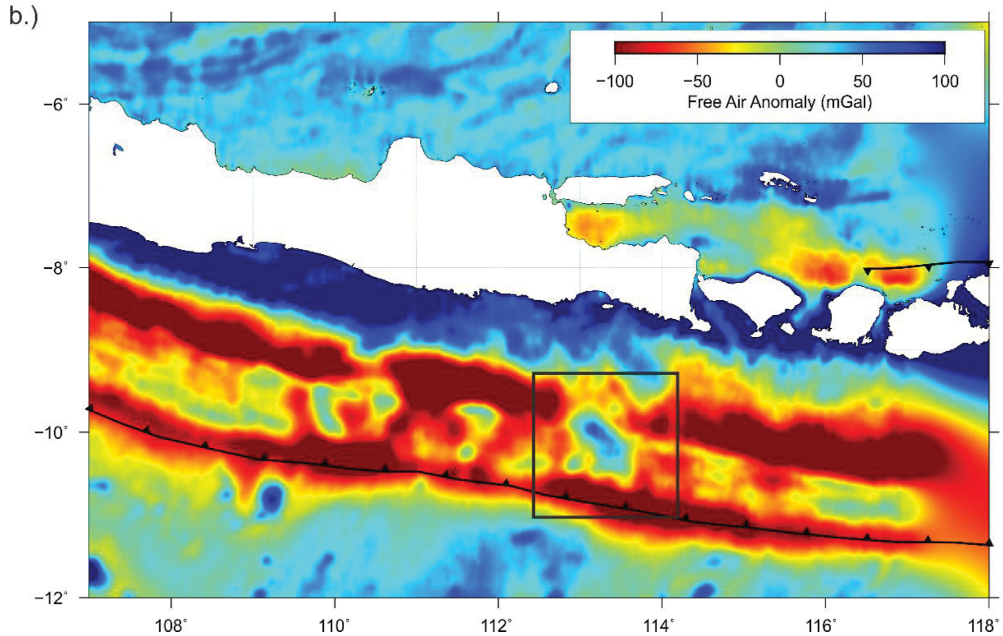

Figure III.10 continued

Meanwhile, the high-velocity anomalies (Vp and Vs) are considerably found at a depth of 10 km in the southern and northern part of the island, which are associated with the positive Bouguer gravity anomaly of the Southern Mountains zone and Rembang zone, respectively (Smyth et al., 2005, 2008; Waltham et al., 2008). It is also consistent with low Vs anomaly in the northern and high-Vs anomaly in southern Java, as indicated by ambient noise tomography (Martha et al., 2017). From 20 km to 30 km, we observe the high-velocity anomaly in southern Java that probably corresponds to the rigid forearc, and below 50 km, is associated with the oceanic lithosphere that is subducted toward the north.

We present vertical cross-sections through several areas across the Central and East Java region (Figure III.9) to look at the vertical distribution of velocities with the overlayed seismicity. The locations of the vertical sections are shown in Figure III.1a. The presence of the subducted slab is recognizable, dipping toward the north at depths of about 50 to 100 km, by the high-velocity areas with a low Vp/Vs ratio (e.g., Zhang et al. 2004; Reyners et al. 2006) and is consistent with the delineation of slab model 2.0 (Hayes et al., 2018). The earthquakes are also located in this area with high Vp and Vs to a depth of 150 km along with the slab.

The region below 150 km depth is not well-resolved in our model. According to the tomograms, seismicity, and slab model, the dip of the subducted slab is increasing with depth toward the north, as suggested by previous studies (Fukao et al., 1992; Koulakov et al., 2007; Zenonos et al., 2019). However, the thickness and geometry of the slab are hard to estimate precisely from tomographic images. Fine structures of the subduction slab can be further studied by a dense seismic network, in particular, the ocean-bottom-seismometer (OBS) network (Zhao, 2015). Meanwhile, low-velocity zones above the top limit of the subducted slab are likely to be found at ~100 km depth as the possible location of partial melting zones. Thermal models of the Java subduction zone also estimate the transition depths (from the decoupling to coupling between the slab and the overriding mantle) of about 80-155 km with the maximum temperature at the transition zone and the mantle wedge beneath the volcanic arc up to 693ºC and 1458ºC, respectively (Syracuse et al., 2010). In such areas, the high-fluid and thermal conditions are probably responsible for this anomaly — the water released from marine sediments and the oceanic crust of the subducted slab before the downgoing slab reaches beneath the volcanic arc. Fluids from this slab dehydration and temperature increase in the mantle wedge due to the heat convection from the deeper part of structure, lead to partial melting. Thus, seismic velocity is significantly lower relative to surrounding dry areas (Syracuse et al., 2010; Tonegawa et al., 2017; Zhao, 2015).

As previously mentioned, low-velocity anomalies with high Vp/Vs ratio are observed beneath the volcanic complexes, especially seen in the vertical sections. In Figure III.9a, where the vertical section A-A' slices the Mt. Merapi-Merbabu complex, we see low-velocities (Vp and Vs) at a depth of 20 km. It is probably associated with the magmatism beneath Mt. Merapi or Kendeng sedimentary basin, as also represented by previous local tomographic studies in the same area (Koulakov et al., 2007; Luehr et al., 2013; Ramdhan et al., 2019; Wagner et al., 2007). Mt. Merapi is one of the most active volcanoes in the world, with an eruption cycle of two to six years and large eruptions occur every 50 to 100 years (Luehr et al., 2013; Ramdhan et al., 2019). Ramdhan et al. (2019) has imaged the internal structures of Mt. Merapi and determined two anomalies that are interpreted as shallow and intermediate magma bodies at depths of 5 and 15 km, respectively. The presence of these two magma bodies cannot be distinguished by the resolution of our tomography. However, our velocity models may depict the partial melting zone at a depth of ~100 km, indicated by low-Vp and Vs. The ascending fluids and melts migrate upward from the slab and concentrate beneath the volcanic front, supplying magma to the active volcanoes. Koulakov et al. (2007), Wagner et al. (2007), and Luehr et al. (2013) also highlight the prominent feature of Merapi-Lawu anomaly (MLA), as the strong low-velocity anomaly situated close to the Mt. Merapi and extendings to Mt. Lawu in the east. They discuss the origin of the MLA feature that is partly caused by thick lava and sedimentary deposits in the Kendeng basin which correlates with a negative gravity anomaly.

In the central part of the study area, Figure III.9b shows vertical section B-B' through Mt. Wilis-Pandan. A low-Vp and Vs anomaly with a high Vp/Vs ratio down to a depth 30 km beneath Mt.Pandan is probably associated with a location of magma, and its movement toward the surface can be related to the earthquake clusters. Mt. Pandan is defined as a dormant volcano north of Mt. Wilis and close to the Kendeng thrust fault. Mt. Pandan is not listed as an active volcano, and it is unclear whether the local earthquakes are associated with the Kendeng thrust activity or magmatic activity. A gravity survey has been conducted to delineate the internal structure of Mt. Pandan and link it to the earthquakes sequence around the region (Santoso et al., 2018). The map of Bouguer anomalies shows low-density value beneath Mt. Pandan that may be related to a weak zone, hot materials, or magma source. Santoso et al. (2018) suggested that the subduction process triggers the fault movement and, at the same time, triggers the ascending magma to the surface.

In the eastern part of the study area, the volcanoes are distributed relatively close to each other. Most of the volcanic areas show features of low velocities that are interpreted to be regions of fluids and magma. In Figure III.9c, section C-C' slices through Mt. Semeru-Bromo. Low-velocity anomalies with high Vp/Vs are observed at ~ 50 km depth beneath the volcanoes. The section D-D' in Figure III.9d, which passes through Mt. Ijen-Baluran in the easternmost Java, shows a low-velocity anomaly with a high Vp/Vs ratio from ~50 km depth beneath the volcano, and the wedge also appears to be associated with a low Vp/Vs ratio. The interaction between the volcanic and sedimentary domains is concentrated at the surface in East Java, producing sediment-hosted geothermal system and clastic-dominated geyser-like eruption (nicknamed Lusi-Lumpur Sidoarjo) (Fallahi et al., 2017; Lupi et al., 2022). The plumbing system that feeds Lusi has been proposed by several tomographic studies in the region (e.g. Fallahi et al., 2017; Karyono et al., 2020; Lupi et al., 2022), suggesting that the magmatic system of Lusi connects to the surrounding volcanoes (Mt. Penanggungan and Mt. Arjuno-Welirang complex. The plate subduction promotes the formation of thrust faults below the volcanic arc. Magma and fluids originating from volcanic complex migrate through the weakened rocks along the fault system to the sedimentary basin, manifesting in the sediment-hosted geothermal system of Lusi. Furthermore, our results depict the partial melts feature at ~ 100 km depth above the slab that is indicated by a low-velocity anomaly with a high Vp/Vs ratio. The partial melting is promoted by joint effects between heat convection in the mantle wedge and fluids from slab dehydration beneath the volcanic arc, producing magmatism in the region (Zhao et al., 2012).

Based on the Vp models, we present the interpretative cross-sections in Figure III.11 for the Central and East Java region. As the oceanic Indo-Australia plate moves northward and subducts beneath the Eurasian plate, partial melting occurs at a depth of about 100 km. Fluids and melts are ascending to the surface and feeding the volcanoes located above the low-velocity anomalies. We realize that our tomographic results might have limitations in producing smooth images. Some features can be observed in certain sections while not seen in other sections. We expect that the main factor is the limitation of the ray coverage. The station distribution used in this study is relatively sparse, and path distribution can also be highly heterogeneous. Model parameterization with an irregular grid may be adapted to improve the stability of inversion and extractions of structural information beneath Central and East Java in further studies, as described by Rawlinson et al. (2014).

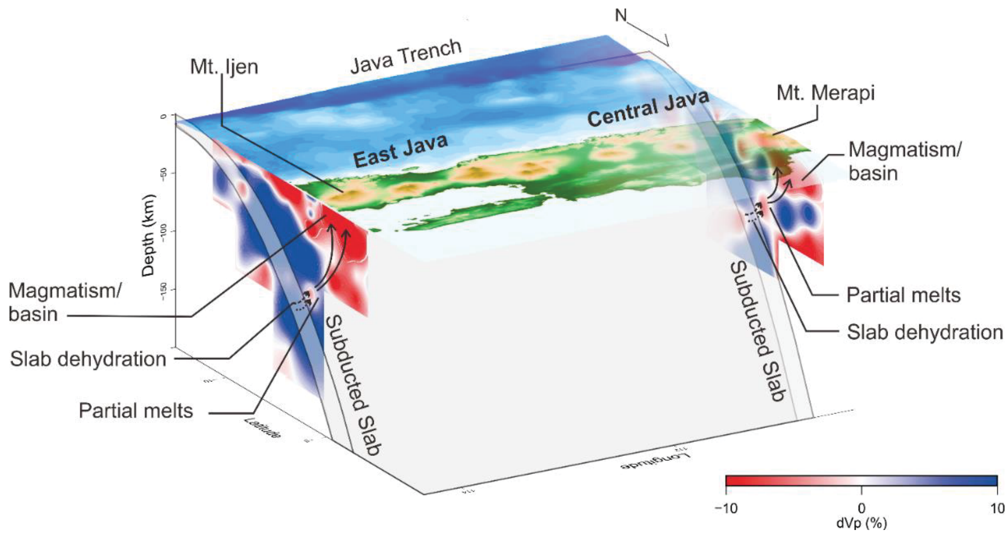

Figure III.11 Interpretative cross-sections of the velocity structure from Vp beneath Central and East Java subduction zone. The tomography cross sections show Vp distributions which pass through Mt. Merapi-Merbabu and Mt. Ijen.

III.6 The relationship to Recent Large Earthquakes

Inland faults contribute to the potential seismic hazard in the region since they have been recognized as active structures based on geological and geodetic studies (Marliyani, 2016; Pusat Studi Gempa Nasional (PuSGeN), 2017), but some faults do not show a significant rate of recent seismicity. On the other hand, we observed shallow clustered earthquakes near the Opak fault, Central Java region. The activity of Opak fault is considered to be the cause of the 2006 Yogyakarta earthquake (Mw 6.3), with latitude, longitude, and depth of 8.04^{o}S, 110.36^{o}E, 15 km, respectively (International Seismological Centre, 2021) (http://www.isc.ac.uk/). The focal mechanism from the Global Centroid Moment Tensor (GCMT) (https://www.globalcmt.org/) (Dziewonski et al., 1981; Ekström et al., 2012) shows a strike-slip faulting mechanism with strike in the NE-SW direction. Figure III.12b represents a vertical section of the tomographic model across the fault, along with the clustered earthquakes in the period of our observation, with depths less than 20 km. These earthquakes are located in the contrast of seismic velocities, reflecting the existence of different types of lithology. It is consistent with previous tomographic studies (e.g., Rohadi et al., 2013; Ramdhan et al., 2017; Diambama et al., 2019), and they suggested that low-velocity anomaly is associated with carbonates or other sedimentary rocks that overly the Oligo-Miocene volcanic deposits characterized by the high-velocity. However, we need to conduct a higher resolution of tomography in order to better image small-scale anomalies around the fault. This can be achieved by increasing the density of ray path coverage between the local earthquake and seismic stations and grid nodes refinement. At least, we can infer from our results that the geometry of Opak fault is dipping to the east, which supports the previous result of Tsuji (2009) and Diambama (2019).

The recent study of Widiyantoro et al. (2020) has revealed the seismic gaps south of Java, one of which is in the Central and East Java region. The lack of recent megathrust events may indicate great tsunamigenic earthquakes (Mw8.8) can be possible with return periods of about 400 years. The latest tsunami earthquake in the region is the 1994 Banyuwangi earthquake (Mw 7.8), with the latitude, longitude, and depth of 10.48ºS, 112.91ºE, 32.1 km, respectively (International Seismological Centre, 2021). A thrusting fault mechanism is indicated for the mainshock (https://www.globalcmt.org/) (Dziewonski et al., 1981; Ekström et al., 2012), but the aftershocks are dominated by normal faulting (Abercrombie et al., 2001). They interpreted the observations as a mainshock that slipped over a subducted seamount, which produced normal faulting aftershocks at the outer rise of the Indo-Australian plate.

On 10 April 2021, a Mw 6.1 earthquake occurred near Malang, East Java, without triggering a tsunami for the coastal area of southern Java. However, the event produced strong shaking with MMI V in the East Java area, according to the shakemap reported by BMKG, causing building damage and fatalities (http://shakemap.bmkg.go.id/). The preliminary report of the hypocenter location is at 8.84ºS, 112.47ºE with a depth of 86 km (http://repogempa.bmkg.go.id/) with a thrust fault mechanism. To better constrain the event location, we have manually re-picked the mainshock arrivals from 19 stations (Appendix D) and determined the hypocenter by applying a non-linear method (Lomax et al., 2000). We plotted the wadati diagram to see the linearity between the phases and obtained a Vp/Vs ratio of 1.75 (Appendix D). Finally, we have updated the hypocenter location of the 2021 Malang earthquake (Mw 6.1) at 8.94ºS, 112.45ºE with a depth of 59.7 km and included the result on our tomographic models. The hypocentral errors for the event are 3.08, 6.39 and 11.91 km in x, y and z directions, respectively.

Figure III.12c shows the vertical section of the velocity model across the 1994 and 2021 events. Both events are located on the high-velocity region associated with the geometry of the oceanic slab that steepens towards the north. Seismic clusters of our data period are also located relatively close to the 2021 event and provide the location of the rupture area in this region. Any ground shaking caused by large magnitude earthquakes will be a threat to the population of Java, although without triggering a tsunami. Meanwhile, the area near the 1994 event lacks thrust events since it is the location of the seismic gap. At ~ 50 km depth, a low-velocity anomaly exists at the boundary of the subducted slab with a ~50 km width and extends to the depth of ~25 km. This feature may exhibit the presence of subducted seamount that were previously acknowledged by Abercrombie et al. (2001). Seamounts off Java have been initially recognized in early side-scan sonar along the eastern Java Trench (Masson et al., 1990) and revisited by multichannel seismic reflection profiles and multibeam bathymetric data (Kopp et al., 2006, 2011; Xia et al., 2021). Some of these seamounts are currently being subducted and causing uplift of the forearc to the shallower water depth (Figure S16). In the area of 1994 earthquake, a large subducting seamount modulates the seafloor bathymetry (Xia et al., 2021) and is manifested in the isolated free-air gravity anomaly close to the trench (Sandwell et al., 2014) (black square in Figure 6b). Based on these observations, Xia et al. (2021) suggest that the seamount has a height of ~ 2 km and a possible width of ~ 40-60 km. However, our resolution with grid spacings of 50 km and 10 km in lateral and vertical variations, respectively, does not allow us to estimate the true dimension of this subducted seamount. Similar features of subducting seamounts indicated by low-V zones are also observed in the Pacific slab beneath Kanto, Japan with a ~ 30 km width (Nakajima and Hasegawa, 2006) and Cocos slab beneath Costa Rica at 30 km depth (Dinc et al., 2010; Husen et al., 2003) and are associated with more hydrated regions compared to the surrounding slab. A possible location of partial melting is observed at a depth of 100 km, indicated by a low-velocity anomaly with a high Vp/Vs ratio. Fluids from slab dehydration and the temperature increase in the mantle wedge promote the partial melting in the area. The fluids/melts then ascend from the mantle wedge to feed volcanoes at the surface.

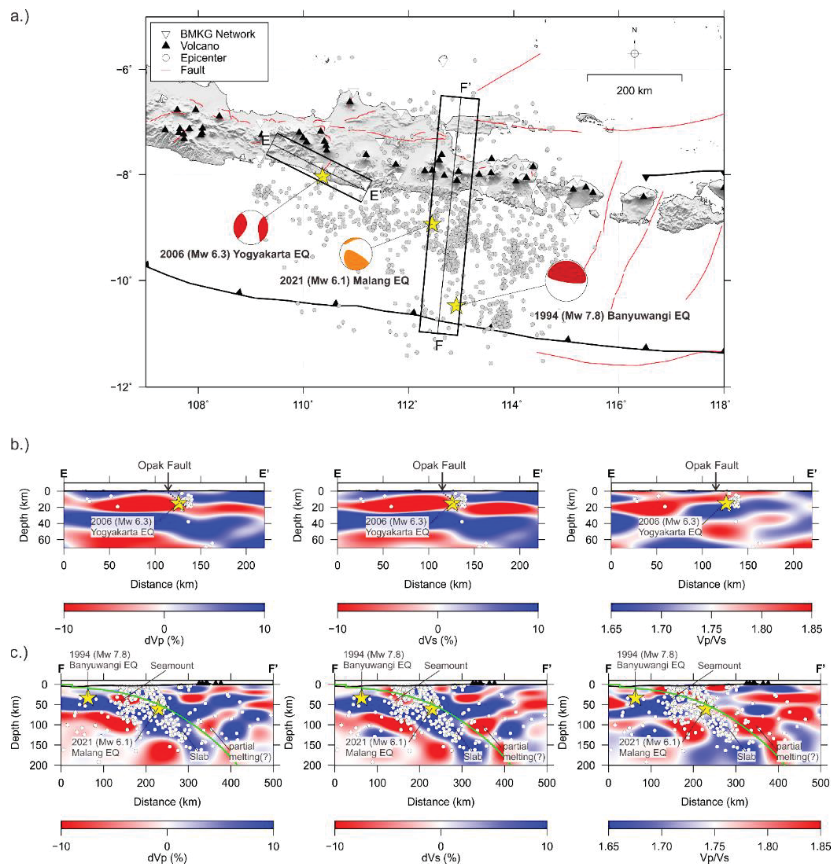

Figure III.12 (a) Map of the large earthquake epicenters (yellow stars) and the seismicity (gray circles) used in this study. Focal mechanism solutions are taken from GCMT ((https://www.globalcmt.org/) Two bottom figures are vertical sections for Vp, Vs and Vp/Vs ratio with relocated seismicity across (b) the 2006 Yogyakarta earthquake (Mw 6.3) (E-E'), (c) the 1994 Banyuwangi earthquake (Mw 7.8) and the 2021 Malang earthquake (F-F').

Chapter IV Crustal Anisotropy in Central and East Java Region, Indonesia based on Shear Wave Splitting Analysis

IV.1 Data

We investigated shear wave splitting using seismograms from 30 broadband stations of BMKG within the time period of 2009-2020 and local S phases. The earthquake catalog was derived from Muttaqy et al. (2021 - in review) and BMKG (http://repogempa.bmkg.go.id/) for the events in 2009-2017 and 2018-2020, respectively. We constrained the earthquake data to the criteria of a crustal anisotropy study, i.e. event depths less than 30 km with a radius of 150 km from each recorded station (Figure IV.1). The restriction was considered based on the crustal thickness in Central Java inferred from Wölbern and Rümpker (2016) using P receiver functions.

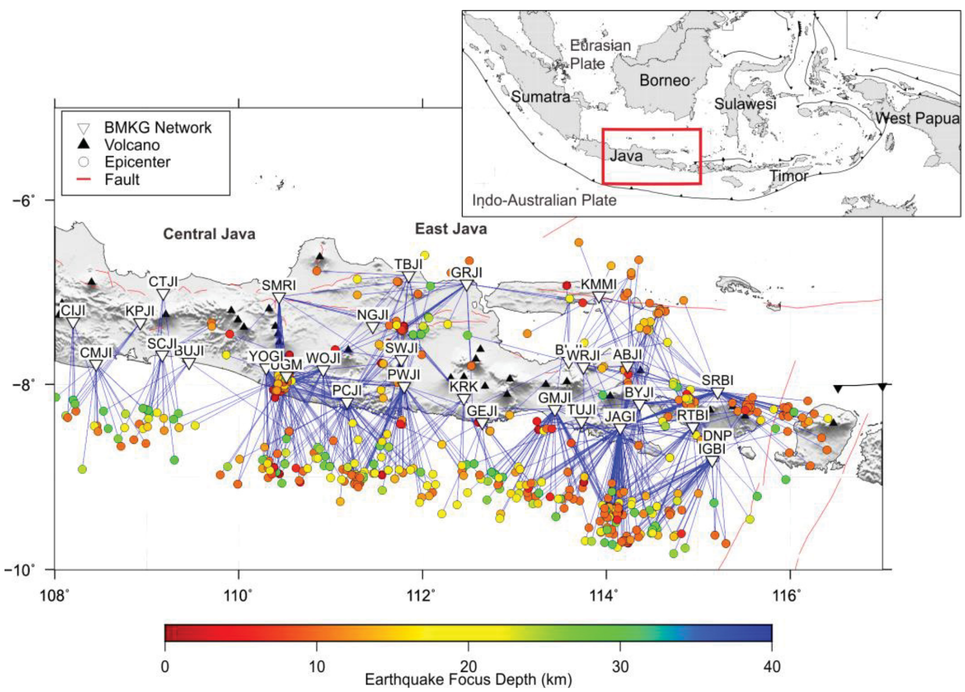

Figure IV.1 Map of ray paths distribution that connect seismicity and stations used for the splitting measurements in Central and East Java region.

For shallow earthquakes that emitting the rays at low angles to the surface, the S-P converted waves may contaminate the splitting measurements. Thus, we sorted the rays with incidence angle steeper than 40º as most shear wave splitting studies use (e.g., Balfour et al., 2012; Collings et al., 2013; Savage et al., 2016; Syuhada et al., 2017) which were calculated using TauP Toolkit (Crotwell et al., 1999) with an average global 1-D velocity model of ak135 (Kennett et al., 1995) for every single station. Once the input data is ready, we then performed an automatic shear wave splitting algorithm of MFAST package (Savage et al., 2010) that adapts both the SC91 method (Silver and Chan, 1991) and cluster analysis method (Teanby et al., 2004).

In this study, the splitting measurement routine has few requirements beyond the seismograms. The S arrivals need to be included in SAC headers along with other information such as station and event location. For E, N, Z components, the SAC data triplets should start at the same absolute time and therefore need to be synchronized. A few of our seismograms have to be downsampled or cut to prevent program crashes because the cluster analysis program can handle a maximum of 10,000 samples (Teanby et al., 2004). All of the data preparation was done by Obspy Toolbox on python (Beyreuther et al., 2010). Once the input data is ready, we then performed an automatic shear wave splitting algorithm of MFAST package (Savage et al., 2010) that adapts both the SC91 method (Silver and Chan, 1991) and cluster analysis method (Teanby et al., 2004).

IV.2 Filtering and Signal-to-Noise Ratio Calculation

A bandpass filter is used for each measurement based on the signal-to-noise ratio (SNR) criterion and the filter's width to eliminate noise contamination in the raw data. The MFAST package helps the user find the best filter for each measurement, using a predefined set of 14 bandpass filters (Table IV.1). Applying the multiple filters would make this technique applicable to large datasets, with the only manual step is picking the S arrival time (Savage et al., 2010).

A signal-to-noise ratio (SNR) is calculated using the same window length for both noise and signal. The noise window is set before the S arrival (defined as time 0 s) and includes an offset to consider possible inaccuracies of S arrival times (-3.05 to -0.05 s). In comparison, the signal window follows the S arrival (0.05 to 3.05 s). The mean amplitude ratio from the fast fourier transform of the signal and noise windows is used as the SNR. The minimum SNR of each measurement is no less than 3 for further analysis and interpretation.

Table IV.1 Set of the bandpass filter in MFAST package (Savage et al., 2010)

Filter Number	Low Frequency (Hz)	High Frequency (Hz)	Bandwidth (Octave)
1	0.4	4	5
2	0.5	5	5
3	0.2	3	7.5
4	0.3	3	5
5	0.5	4	4
6	0.6	3	2.5
7	0.8	6	3.75
8	1	3	1.5
9	1	5	2.5
10	1	8	4
11	2	3	0.75
12	2	6	1.5
13	3	8	1.3
14	4	10	1.25

IV.3 Splitting Measurement

The shear wave splitting parameters are measured by applying an inverse splitting operator, determined by a grid search over possible values (Silver and Chan, 1991). The more a specific operator removes the splitting of the investigated waveform, the smaller the eigenvalue λ_2 of the covariance matrix of particle motion $c(\phi, dt)$ becomes. This is equivalent to maximizing linearity of the particle motion (Silver and Chan, 1991). The inverse operator that removes the shear wave splitting best gives the resultant shear-wave splitting parameters. Contours of λ_2 for all the operators considered give a measure of confidence region using an F-test (SC91) (Figure IV.2f and IV.3f). Teanby et al. (2004) proposed the cluster analysis method to automatically perform measurements for many window configurations and then determine the most stable solution. In the

MFAST package, it generates a customized configuration file for every single measurement automatically. Measurement window times relative to the S-arrival are calculated based on the dominant frequency of the signal.

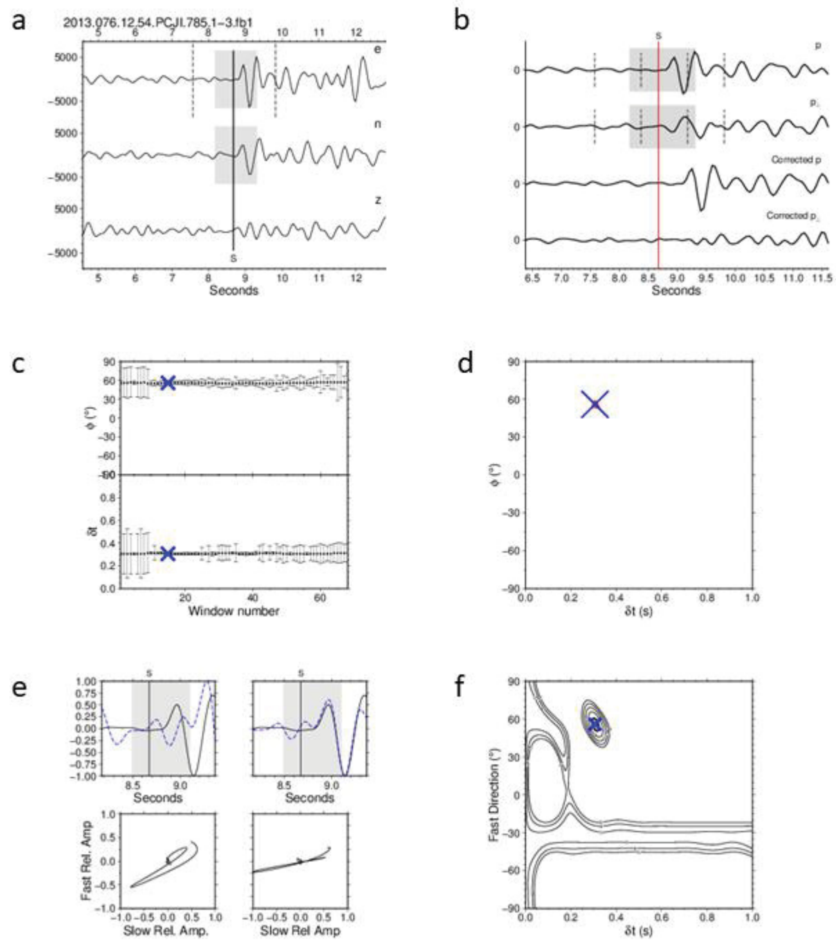

Figure IV.2 High-quality, A-grade measurement recorded at station PCJI for 17 March 2013 event. (a) Filtered E,N,Z waveforms. The solid vertical line is the S arrival. The dashed lines are the minimum start and maximum end times for windows used in the processing, as Figure IV.2b (b) The waveforms rotated into the SC91-determined incoming polarization direction (p) and its perpendicular value ($p^{\perp}$) for the original filtered waveform (top two curves) and the waveforms corrected for the SC91-determined dt (bottom two curves) for the window shown in grey. (c) Values of ϕ and dt determined for each measurement window as a function of window number. (d) All the clusters of five or more measurements, with the large cross being the chosen cluster. (e) The (top) waveforms and (bottom) particle motion for the (left) original and (right) corrected waveform according to the final chosen SC91 window. (f) Contours of the smallest eigenvalue of the covariance matrix for the final chosen SC91 measurement.

Several sets of statistics describe the clusters, and the most crucial one is the total variance of each cluster. First, the cluster with the minimum variance is decided as the best cluster. Then, within that cluster, the measurement with the minimum variance is decided as the best measurement, and it is used as the final measurement for that phase at that filter (Savage et al., 2010).

IV.4 Grading Criteria

As part of the advance in using the MFAST package, an automatic grading is carried out to determine the best measurement. Instead of simply using the results from the best cluster defined by Teanby et al. (2004) method, all clusters with measurement numbers above the minimum threshold are compared to the chosen ”best cluster”. Let $var(k)$, $\phi(k)$, $dt(k)$ and $Nmeas(k)$ be the average variance, fast polarization, delay time, and number of measurements in cluster k, respectively. Let $kbest$ be the cluster number of the measurement with $var(kbest)$=min($var(k)$), according to the Teanby et al (2004) method. In order to consider clusters of similar quality, the cluster grading considers all clusters with $var(k) < 5 * var(kbest)$ and within these clusters, it considers the differences between the fast polarizations and delay times of each cluster compared to the “best cluster”. Table IV.2 describes a description of the cluster grading methods. Figure IV.2 and IV.3 represent the difference between high and low grade of splitting measurements. A final grade of A and B is made on the basis of whether the measurment has a cluster grade of Acl or Bcl, and values of SNR and 95% confidence interval of the ϕ measurement.

Table IV.2 Quality Criteria in MFAST package (Savage et al., 2010)

Grade Name	Criterion
N (null)	If the polarization ϕ is between -20 to 20 or 70 to 100 degrees of the incoming polarization
Dcl	Cluster D grade: if there is any cluster k for which the following holds: n $meas(k) > Nmeas(kbest)/2$ and $var(k) < 5 * var(kbest)$ and also $tdiff(k) > tlagmax/4$ or $\pi/4 < \phi diff(k) < 3\pi/4$
Ccl	Cluster C grade: if the cluster is not D grade and there is any cluster k for which the following holds: n $meas(k) > Nmeas(kbest)/2$ and $var(k) < 5 *$

	$var(kbest)$ and also $tdiff(k) > tlagmax/8$ or $\pi/8 < \phi diff(k) < 7\pi/8$
Bcl	Cluster B grade: if the cluster is not D or C grade and there is any cluster k for which the following holds: $var(k) < 5 * var(kbest)$ and n $meas(k) > Ncmin$ and also $tdiff(k) > tlagmax/8$ or $\pi/8 < \phi diff(k) < 7\pi/8$
Acl	Cluster A grade: if the cluster is not D, C, or B grade
B	Cluster B, not null, $dt < 0.8 * tlagmax$, $SNR > 3$, $d\phi < 25$
A	Cluster A, $dt < 0.8 * tlagmax$, $SNR > 4$, $d\phi < 10$

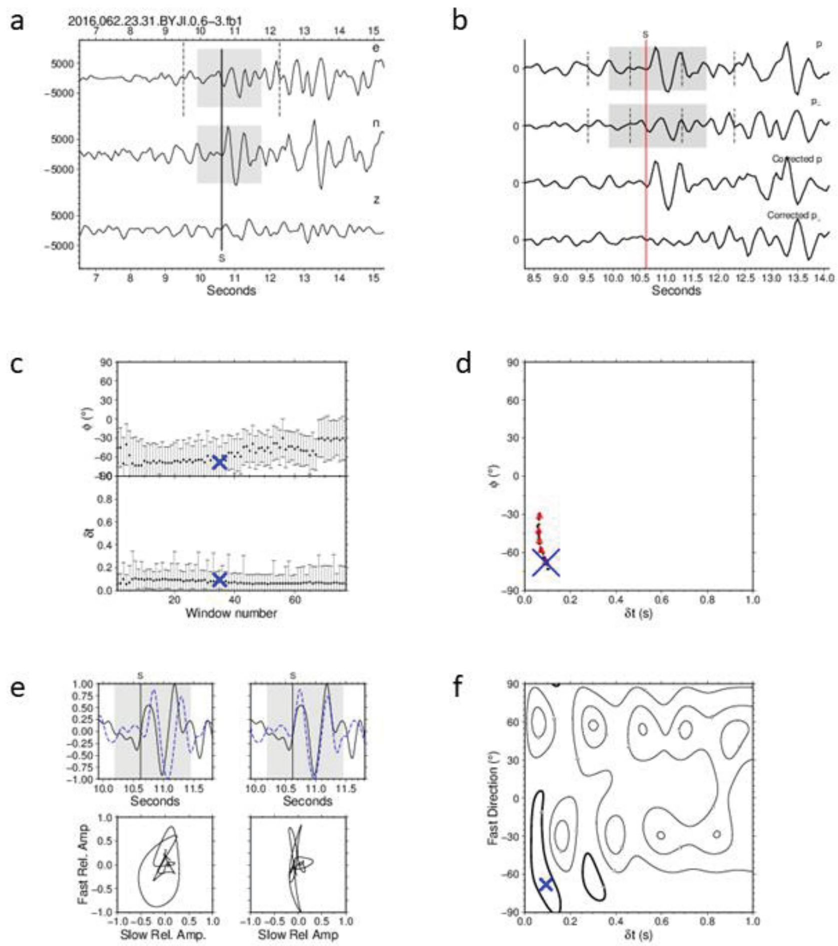

Figure IV.3 Sample C quality measurement, as in Figure IV.2

IV.5 2-D Delay Time Tomography and Spatial Averages

To infer the spatial distribution of splitting results, we use the 2-D delay time tomography and a spatial averaging technique (TESSA) of Johnson et al. (2011). The code computes the first-order approximation of lateral variation in anisotropy without taking depth variations into account and constrains the high and low anisotropy regions. The delay time (δt) from a single measurement is assumed to be accumulated along the raypath from source to the station, and it is proportional to the path length of the ray through the anisotropic medium (Silver, 1996). Then the total anisotropy calculated by TESSA is simply the summation of δt for each grid block in lateral direction (Johnson et al., 2011; Karalliyadda and Savage, 2013). The strength of anisotropy for each block (S_b) is estimated using medium-scale optimisation inversion function in MATLAB that finds the linear least-square solution of the problem, iteratively. It then converges to a final solution for the strength of anisotropy of the whole ray (S_r) within the boundary constrains. The constraints are applied so that the minimum S_r will always be above 0 s/km and the maximum S_r will be less than $\delta t_{r(\max)}/L_b$, where $\delta t_{r(\max)}$ is the maximum delay time (δt) observed along a raypath and L_b is the grid size. The method assumes that δt is simplification of a non-linear relationship between heterogeneous anisotropy and the observed apparent δt at the surface and does not accont for depth dependence of the anisotropy (Johnson et al., 2011; Savage et al., 2016). We used regular gridding with the size of 25 km and set the minimum number of rays to be 5 so if there are no rays travel through a box, the box will not be included for the calculation (Figure IV.4).

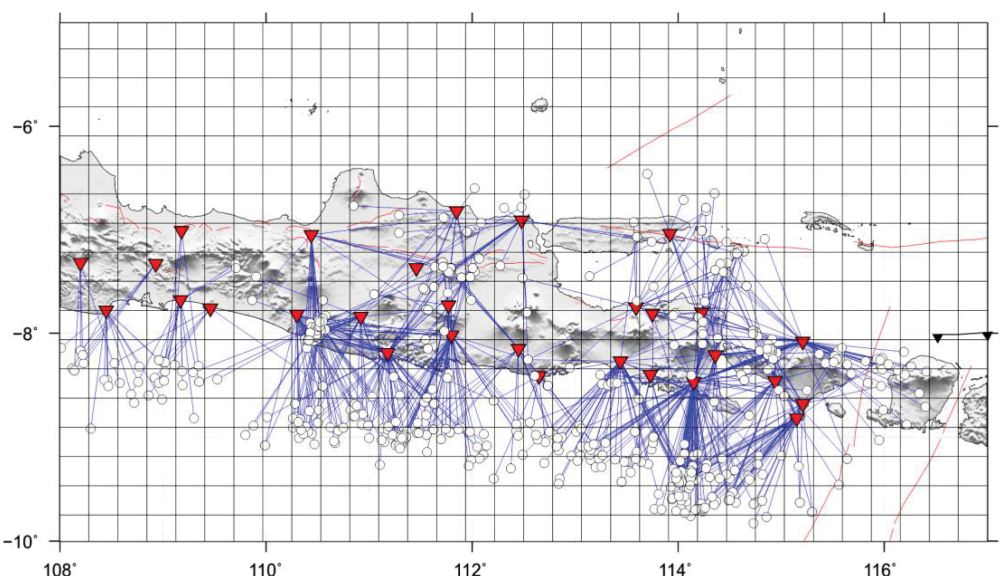

Figure IV.4 Grid and ray paths (blue lines) distribution used in the TESSA inversion. White circles and red inverted triangles are epicenters and stations, respectively.

A checkerboard resolution test is performed to assess which region can be resolved by our dataset. It is carried out by constructing the initial checkerboard model with given anisotropy strength values of 0.01 s/km and 0.02 s/km, then adding random noise generated from a standard normal distribution. Synthetic δt measurements are calculated and inverted using the method as previously described. Figure IV.5 displays a result from the checkerboard resolution test. To estimate average ϕ in the defined grid box, the spatial averaging technique used the tomographic weighting method, which considers any variations due to the heterogeneous anisotropic medium. The weighting function (ω_{rb}) is applied on the strength of anisotropy from each grid box (S_b) so the regions with higher strength of anisotropy will have more given weighting value. ω_{rb} is estimated from S_b along the raypath normalised by delay time for that raypath (δt_r).

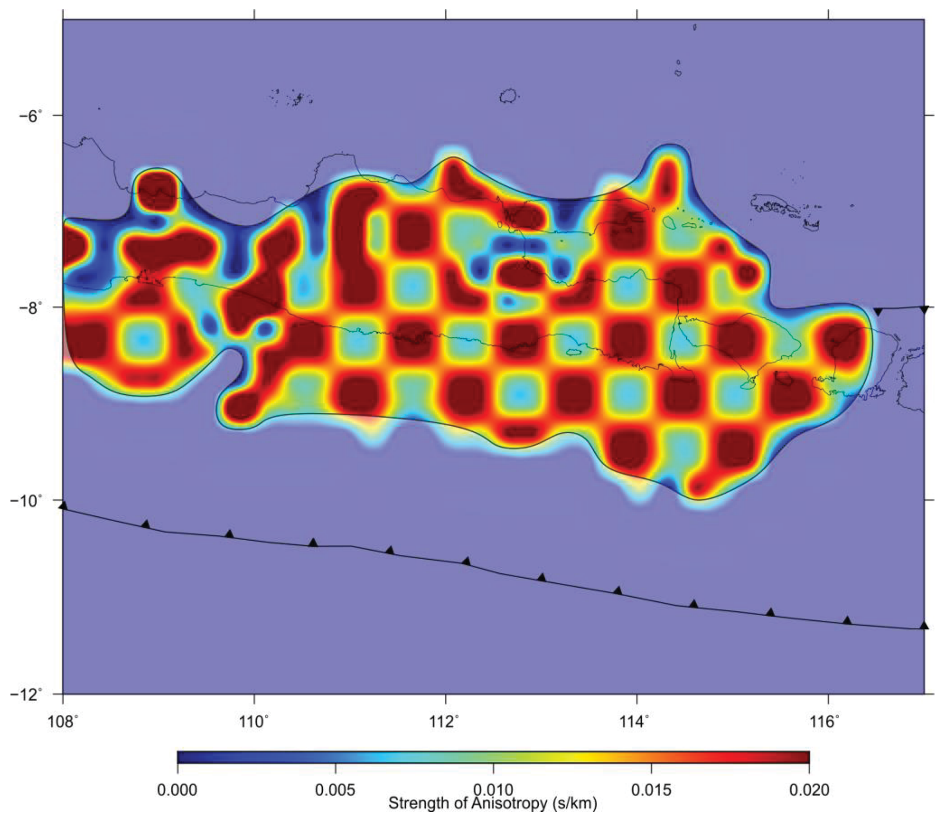

Figure IV.5 Results of the checkerboard resolution test for 2-D δt tomography. Cool and warm colors represent weak and strong anisotropy, respectively.

IV.6 Results

We have obtained a total of 721 splitting measurements with a grade of AB quality at 30 BMKG stations using local earthquakes at focal depths $\leq$ 30 km. Figure IV.6 (a) and (b) show the single splitting parameters distribution and the normalized circular histogram (rose diagrams) of fast polarizations (ϕ) for each station, respectively. To evaluate the quality of splitting parameters, we calculate uncertainties (e.g. mean, standard deviation (SD), standard error (SE)) of the single station measurements using directional statistics of Mardia (1972) and Gerst and Savage (2004) for ϕ. Thus, the errors and accuracy of the average ϕ can be quantitavely estimated. Since the ϕ has a bimodal distribution (180^{o} ambiguity), we need to obtain the parameters i.e. mean ϕ, the length of of the mean resultant vector of ϕ (R), circular standard deviation (CSD) and SE in the directional statistics approach that slightly different from normal statistics. R is a quantitative estimation of circular spread from the mean angular azimuth (ϕ). SE of ϕ is calculated using R and the concentration parameter (κ), which is a Von Mises distribution $V\,M_{(\phi,\kappa)}$. Table IV.3 summarizes the station averages of splitting parameters and its statistical parameters i.e. mean, standard deviation (SD), standard error (SE).

We observe that the fast directions indicate both oblique and perpendicular to the trench. The predominant orientation is NE-SW at most stations in Central Java and almost N-E at stations in central part of East Java and Bali. There is a slight variation of E-W or trench-parallel orientation e.g., at PCJI, KRK, BLJI, GMJI, ABJI stations. Some stations located close to the active fault of Opak (YOGI) and Kendeng (SMRI) have a fault-parallel orientation which probably indicates the structural-induced anisotropy. The activity of Opak fault is responsible for the 2006 Yogyakarta EQ (Mw6.3) while the Kendeng fault is a major fault in Java that extends for 200 km from Central to East Java as an accumulation of thrusts and folds (Pusat Studi Gempa Nasional (PuSGeN), 2017). In addition, the delay times observed at most stations are generally varied within ~0.1 – 0.35 s with exceptional larger δt s at SMRI, KMMI, CTJI and KPJI stations.

Table IV.3 Average results of splitting parameters using the number of shallow earthquakes (N) at each station. Mean ϕ : mean fast azimuth, SE: standard error, CSD: circular standard deviation, R: mean resultant vector of ϕ, mean δt: mean delay time, SD: standard deviation

STA	**N**	**Mean ϕ**	**SE of ϕ**	**CSD of ϕ**	**R**	**Mean δt**	**SE of δt**	**SD of δt**
ABJI	15	80.70	17.96	45.39	0.29	0.23	0.04	0.15
BLJI	16	78.79	39.53	58.13	0.13	0.26	0.04	0.17
BUJI	5	4.40	150.10	67.90	0.06	0.19	0.05	0.11
BYJI	25	51.83	115.25	74.13	0.04	0.33	0.04	0.18
CIJI	4	49.61	8.75	17.70	0.83	0.27	0.05	0.10
CMJI	13	50.80	20.89	46.75	0.26	0.28	0.05	0.16
CTJI	4	59.03	10.70	21.64	0.75	0.37	0.06	0.12
DNP	25	-69.27	30.71	57.72	0.13	0.27	0.04	0.19
GEJI	5	45.84	9.17	20.75	0.77	0.28	0.08	0.19
GMJI	48	83.58	13.27	50.03	0.22	0.19	0.02	0.13
GRJI	21	74.77	19.79	49.81	0.22	0.30	0.05	0.24
IGBI	36	67.08	8.28	39.24	0.39	0.35	0.04	0.24
JAGI	107	62.97	30.91	67.31	0.06	0.27	0.02	0.19
KMMI	9	64.90	24.67	46.45	0.27	0.36	0.07	0.22
KPJI	4	-10.15	13.03	25.87	0.67	0.49	0.04	0.08
KRK	22	-82.49	22.58	52.25	0.19	0.30	0.04	0.17
NGJI	3	56.44	9.78	17.11	0.84	0.26	0.05	0.08
PCJI	56	-83.84	20.43	57.66	0.13	0.25	0.02	0.18
PWJI	44	33.03	47.37	67.09	0.06	0.23	0.03	0.21
RTBI	34	14.58	16.33	50.58	0.21	0.24	0.03	0.15
SCJI	11	38.10	10.71	32.54	0.52	0.22	0.04	0.13
SMRI	19	-80.93	9.35	35.37	0.47	0.36	0.05	0.21
SRBI	60	-37.11	7.98	43.30	0.32	0.23	0.02	0.14
SWJI	17	22.13	21.48	49.43	0.23	0.24	0.04	0.18
TBJI	10	14.45	13.61	36.46	0.44	0.28	0.05	0.14
TUJI	7	-66.14	92.41	63.96	0.08	0.28	0.07	0.18
UGM	40	-84.15	21.85	56.22	0.15	0.28	0.03	0.18
WOJI	29	-62.18	18.50	51.30	0.20	0.24	0.04	0.19
WRJI	4	-72.45	29.42	42.41	0.33	0.30	0.06	0.13
YOGI	28	60.92	13.49	45.83	0.28	0.24	0.02	0.13

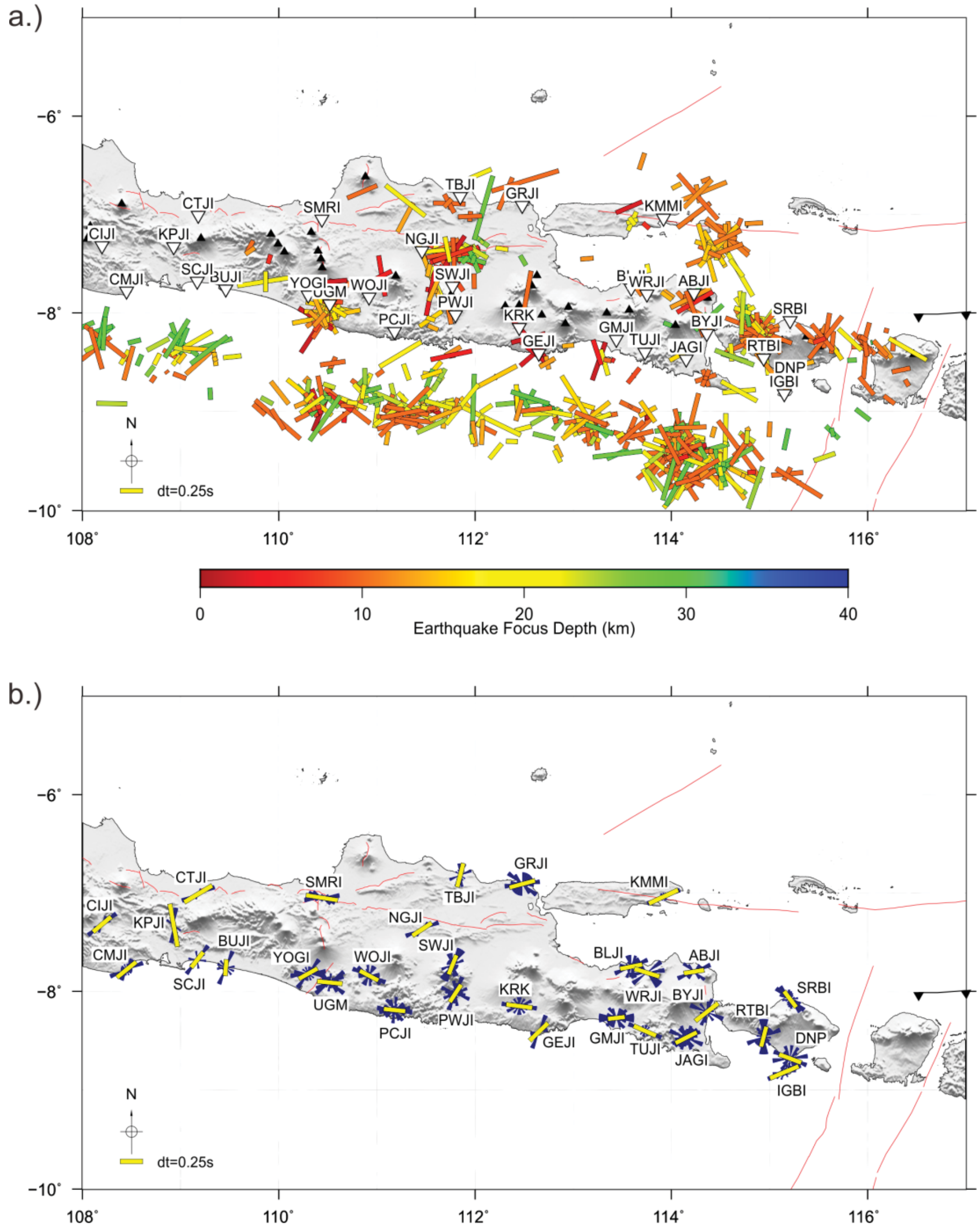

Figure IV.6 Crustal splitting parameters in Central and East Java region for (a) single measurement plotted at the earthquake location and (b) station. Bars orientated in the direction of the fast shear wave polarizations (ϕ), the length of the bar is proportional to the delay times (δt), and the color of the bar represents earthquake focus depth (km) for each measurement. Rose diagrams of fast directions for each station are shown in blue and yellow bars are the average fast direction.

IV.7 Discussion

Figure IV.6 exhibits an inconsistent pattern of splitting results at some closely spaced stations suggesting the occurrence of lateral variations in anisotropy. Thus, the maps of 2-D delay time tomography and the spatial average of fast direction may provide the average anisotropic structure around the region. The 2-D distribution map of δt is shown in Figure IV.7 as the strength of anisotropy (s/km) that constrain strong (red) and weak (blue) anisotropy regions. The shaded region indicates a low resolution and/or large residuals region based on the checkerboard resolution test.

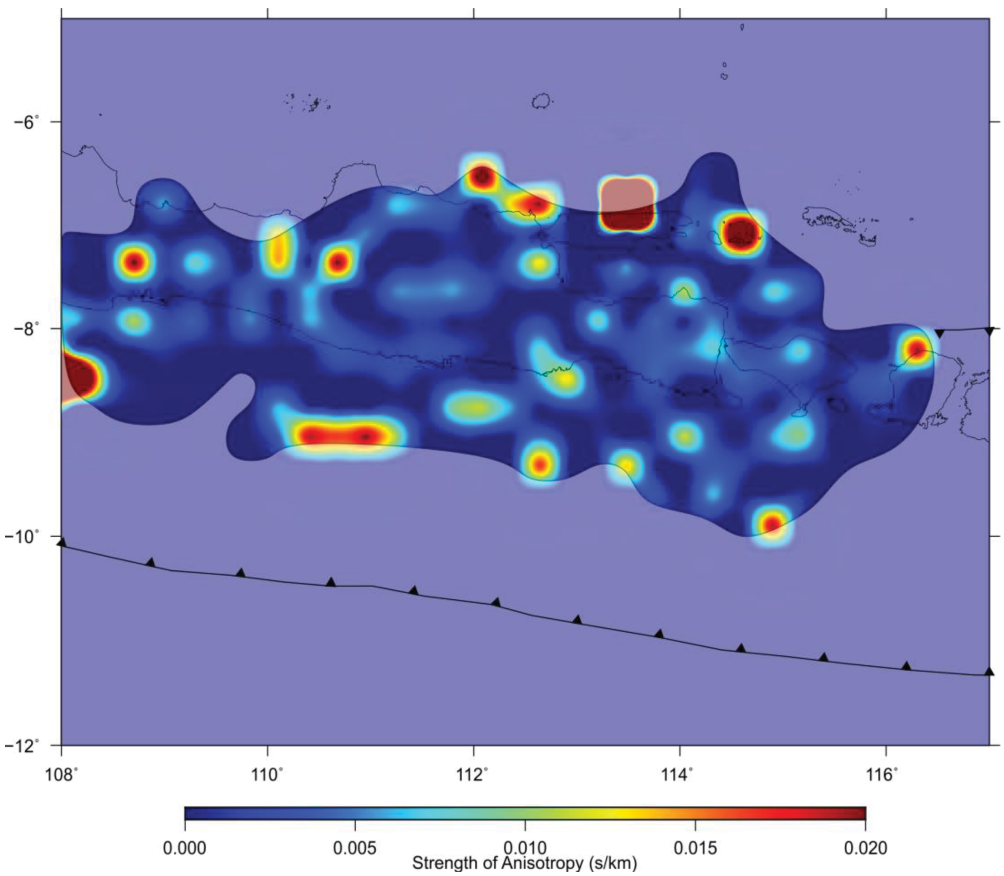

Figure IV.7 2-D delay time tomography inverted from 721 splitting measurements for crustal anisotropy in Central and East Java region. Cool and warm colours represent weak and strong anistropy, respectively.

Moreover, the tomographic weighted average of ϕ obtained for each block is shown in Figure IV.8. We compared the results with the regional strain rate derived from GPS observations of Gunawan and Widiyantoro (2019). The study suggests that Java experiences a large strain rate of more than 1 microstrain/yr. The exceptionally large strain occurs in the northeastern part of Yogyakarta and central part of Central Java which is related to the 2010 volcanic eruption of Merapi. In addition, a large compressional strain is also observed in the Madura Strait where it is most likely due to the activity of the Kendeng Fault (Simandjuntak and Barber, 1996; Smyth et al., 2005). In contrast, the southern part of Central and East Java experiences a small strain rate of less than ~1 microstrain/yr. Based on the characteristic of predominant fast polarization and principal strain rate distributed in Central and East Java, we divided the further analysis into three regions, i.e. (A) Central Java, (B) western East Java, and (C) easternmost Java and Bali region.

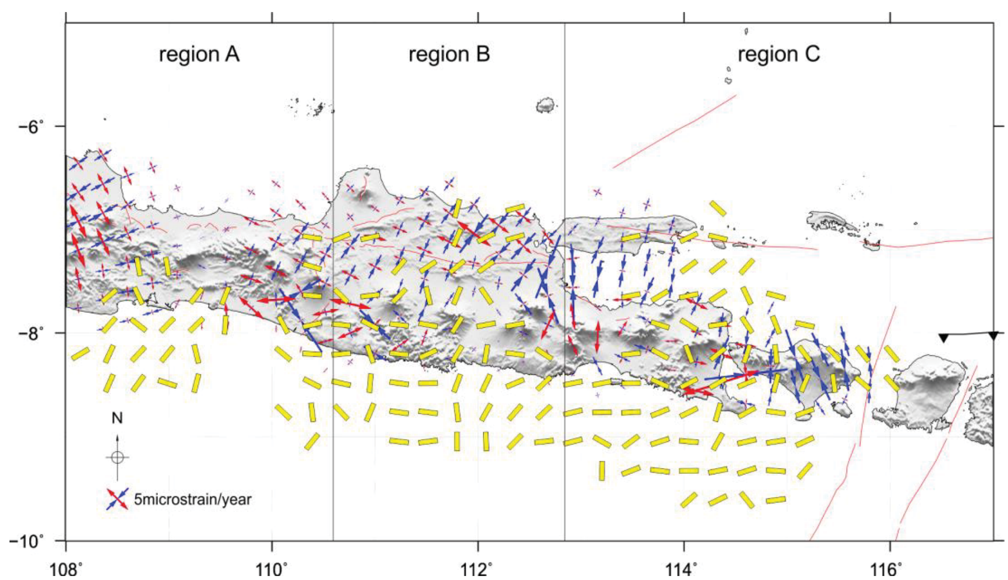

Figure IV.8 Map of spatial distribution of fast direction obtained from TESSA (yellow bars) and strain rate derived from GPS observations (Blue arrows) (Gunawan and Widiyantoro, 2019).

In order to investigate the relationship between depth and anisotropy, we plotted the variations of δt and the normalised value (δt divided by ray path length) with depth for those three regions in Figure IV.9. We then quantified the amount of seismic anisotropy by calculating the percentage of anisotropy (Savage, 1999):

$$\xi = \left[\frac{\delta t \times Vs}{d}\right] \times 100\% \tag{IV.1}$$

where Vs is the average shear wave velocity at the hypocentral depth from the velocity model of Muttaqy et al. (2021), and d is the ray path length. These percentage values are also plotted with depth in Figure IV.9 for every region. We observe that the higher delay times (0.6 to 0.8 s) in Region A are confined at the depth 10-20 km of the crust with the percentage of anisotropy < 4 %, indicating that crustal rocks are not heavily fractured and maintain a high degree of rock integrity allowing the rupture to develop and propagate through them (Crampin and Peacock, 2008). As result, clusterred earthquakes nucleate at < 20 km depths, suggesting the active deformed area.

We suggest that the possible cause of anisotropy in the near Opak fault region is due to the structural-induced anisotropy, resulting in the fast azimuths are oriented parallel to the strike of the structure. The cracks developed in the active fault region may contain fluids at high pore pressure and then becomes perpendicular to the principal strain (Crampin et al., 2002). In the presence of pore-fluid, the fracture criticality of rocks will occur and cause the anisotropy 0.5-10% in the upper crust (e.g. Crampin et al., 1984; Crampin and Booth, 1985). The interpretation is supported by the previous chapter's tomographic images that reveal the low-velocity zone with a high Vp/Vs ratio beneath the Opak fault region (Figure III.9a). This anomaly may reflect some features such as sediments, fluids, or thermal structure ascended from the subducted slab to the surface (Nakajima et al., 2001; Zhao, 2015).

Crustal anisotropy in the overriding plate at the subduction zone is usually caused by cracks and micro-cracks or stress-induced in the upper 10-15 km crust, which results in the aligned fast direction with maximum stress (Crampin, 1994). As shown in Region B, which represents the western part of East Java, the fast directions are considerably parallel to the principal compressional axis of strain rate with maximum shear strain rate vary from 1-5 microstrain/year. They rotate from E-W in the southern part to NE-SW orientation in the northern part, initially suggesting stress-induced anisotropy. There is an area with moderate anisotropy strength of 0.01 s/km in the central part of region B, where also lies the low-velocity anomaly near Merapi and Lawu volcanoes based on the previous velocity tomograms with Vp/Vs ratio 1.9 (Figure III.8). This feature reflects a feeding mechanism for the volcanoes in the region and is related to high content fluids and melts in the crust (Koulakov et al., 2007; Rohadi et al., 2013; Wagner et al., 2007). Another moderate anisotropy strength area is observed in the south of the island where the seismicity is slightly intense and clustered in the forearc region.

Most splitting measurements exhibit the low percentages of anisotropy (<4%) with the normalised δt less than 10 ms/km which indicates that rocks in the upper and lower crust of the region are not heavily fractured (Crampin, 1994). It also suggests that the possible cause of anisotropy is due to stress-induced, providing an anisotropy percentage of about 3-4.5% (e.g. Piccinini et al., 2006). The stress-induced anisotropy is usually existed in the near-surface and slightly decreases at the deeper crust due to high pressure that closing the microcracks. However, the presence of water inclusion may prevent the microcracks to close, contributing to the anisotropy of about 0.5-10 % (e.g. Crampin et al., 1984; Crampin and Booth, 1985; Hiramatsu and Iidaka, 2015). In addition, we observe some large anisotropy strength (0.02 s/km) areas in the south and north of the Island that probably come from the structure at a depth of 10 km. Shallow seismic anisotropy has been attributed not only to faulting structures but also to the alignment of anisotropic minerals along sedimentary layers or metamorphic rocks (e.g. Kaneshima, 1990). The high anisotropic rocks such as gneiss, schist, and amphibole provide a high percentage of anisotropy up to 12% in the laboratory experiment (Okaya et al., 1995).

Our results are consistent with the previous shear wave splitting studies for the stations at the same region (i.e. Di Leo et al., 2012; Hammond et al., 2010). These previous studies have estimated splitting parameters to identify anisotropic medium within the lithosphere and mantle using local and teleseismic events. Hammond et al. (2010) reported both trench parallel and trench perpendicular fast directions for local S-wave splitting in Java. The trench perpendicular is obtained from intermediate-depth events, while shallower and deeper events having more trench parallel fast directions. It suggests the possible cause of crustal anisotropy in this region due to vertically aligned cracks associated with deformation in the overriding Eurasian plate. Another explanation for the trench parallel anisotropy in this region is probably associated with the fossil anisotropy in the slab lithosphere subducting beneath Java. This oceanic lithosphere is older, formed in 80-140 Ma, and plate motions for the Indo-Australian plate between 74-119 Ma are eastward, resulting in trench parallel anisotropy orientation. The oceanic lithosphere subducting Sumatra then formed 40-80 Ma, and the Indo-Australia plate moves northward at this time (Lithgow-Bertelloni and Richards, 1998).

Finally in region C, which represents the easternmost part of East Java and Bali, the fast polarization generally ranges from NW-SE and NE-SW. It indicates strong spatial variations of seismic anisotropy and suggests that this region's crustal structure consists of a complex and non-uniform anisotropic structure with different mechanisms. Some regions, i.e. Madura and Bali, have fast directions parallel and subparallel to the predominant principal strain, suggesting stress-induced anisotropy that caused by cracks and microcracks as a response to the local tectonic stress. Meanwhile, in the area between East Java and Bali, there is a large compressional strain rate observed with E-W orientation which corresponds to the normal faulting mechanism of the Wongsorejo fault as Gunawan and Widiyantoro (2019) suggested. Our results show that the area has almost perpendicular fast directions relative to the principal axis, suggesting that the presence of water inclusion in the cracks may cause structural-induced anisotropy. We observe that the strength of anisotropy is relatively low (< 0.01 s/km) with percent anisotropy below 4% in most splitting measurements. It indicates that the crustal structure in region C consists of rocks that are not heavily fractured (Crampin and Peacock, 2008).

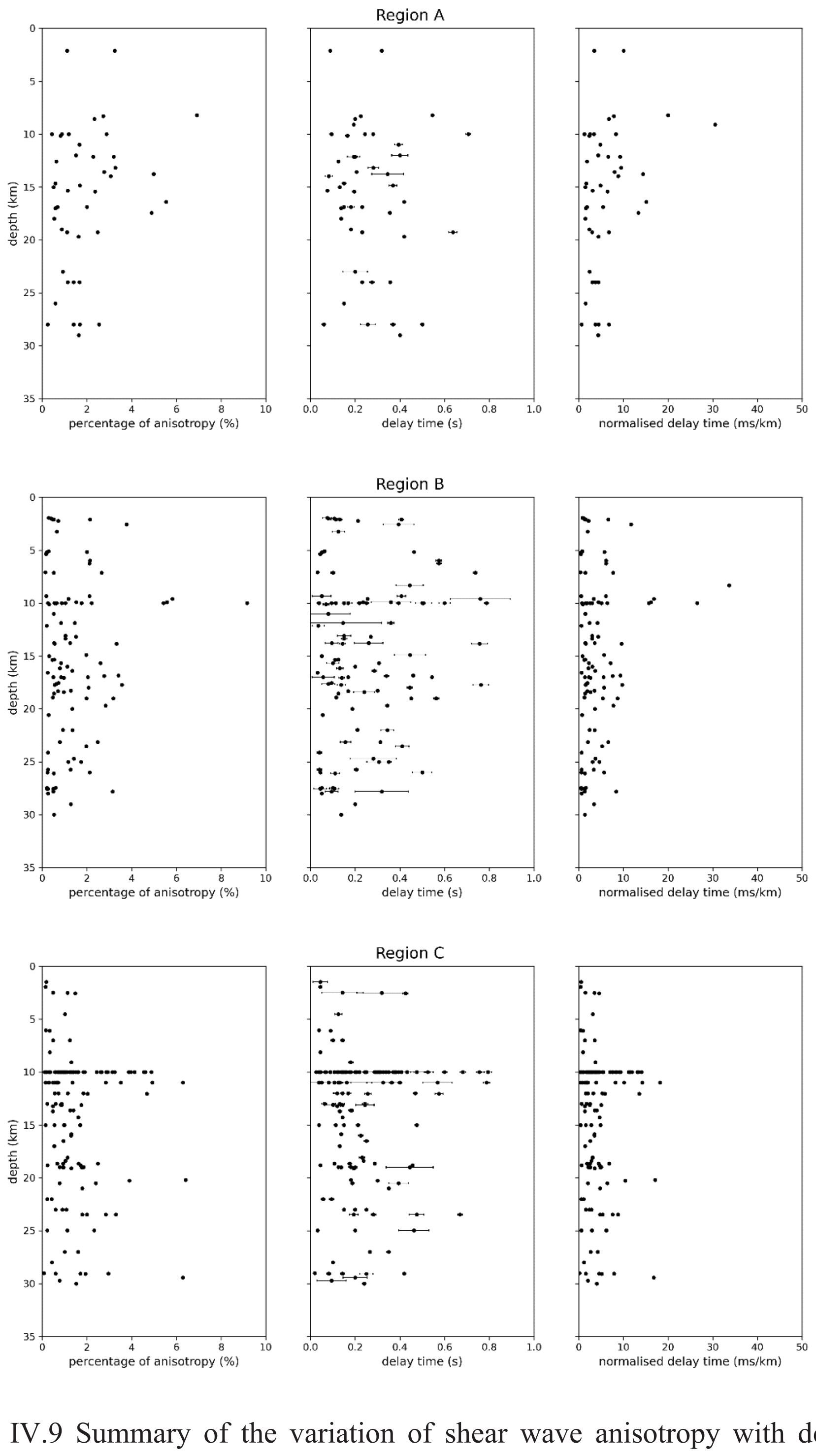

Figure IV.9 Summary of the variation of shear wave anisotropy with depth in region A, B, and C. Left, middle and right panels show plots of percentage of anisotropy, delay time versus depth and normalised delay time, respectively.

Chapter V Upper Mantle Anisotropy in Central and East Java Region, Indonesia from Local Shear Wave Splitting Analysis

V.1 Data

We used waveform data from 38 broadband stations of the Meteorological, Climatological, Geophysical Agency of Indonesia (BMKG) from 2009 to 2020 to determine lithospheric anisotropy structure beneath the Central and East Java region, Indonesia (Figure V.1). The earthquake catalog was derived from Muttaqy et al. (2020 - in review) and BMKG (http://repogempa.bmkg.go.id/) for the events in 2009-2017 and 2018-2020, respectively. We constrained the splitting measurements to the divided region of Central Java (A), western East Java (B), and easternmost East Java (C) with the earthquake depth of 30-300 km, magnitude (Mw) >3, and the epicentral distance less than 300 km from recorded stations (Figure V.2).

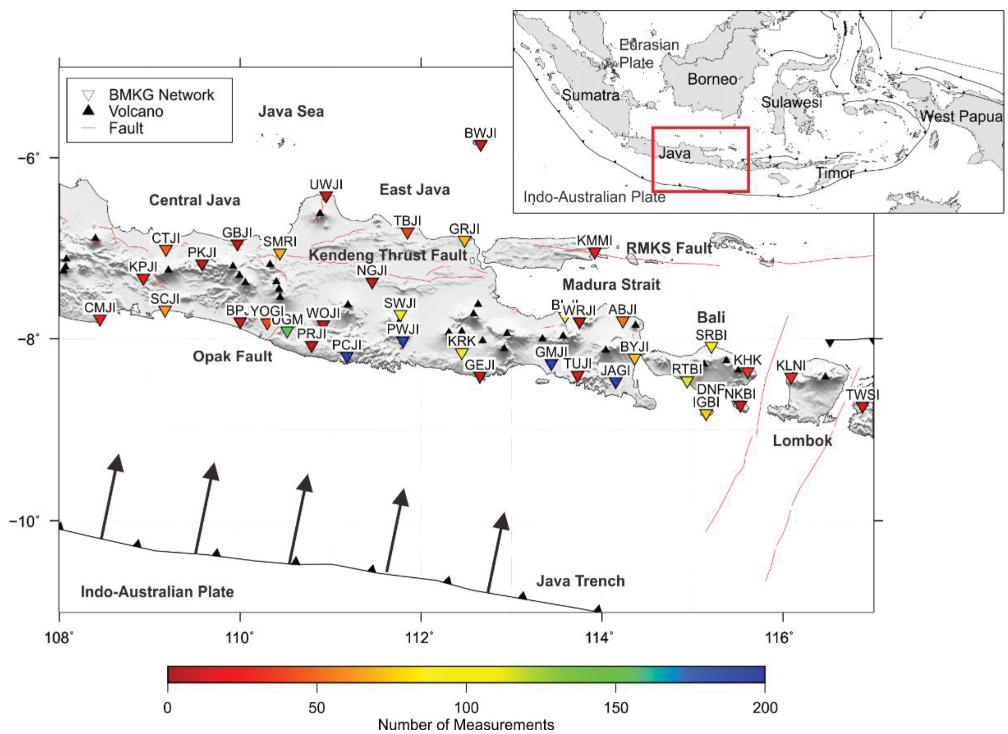

Figure V.1 Map of tectonic setting around Central and East Java region and the main structural features associated with the Java subduction zone. Inverted triangles are the seismographic stations used in the study and the colors represent the number of measurements for each station.

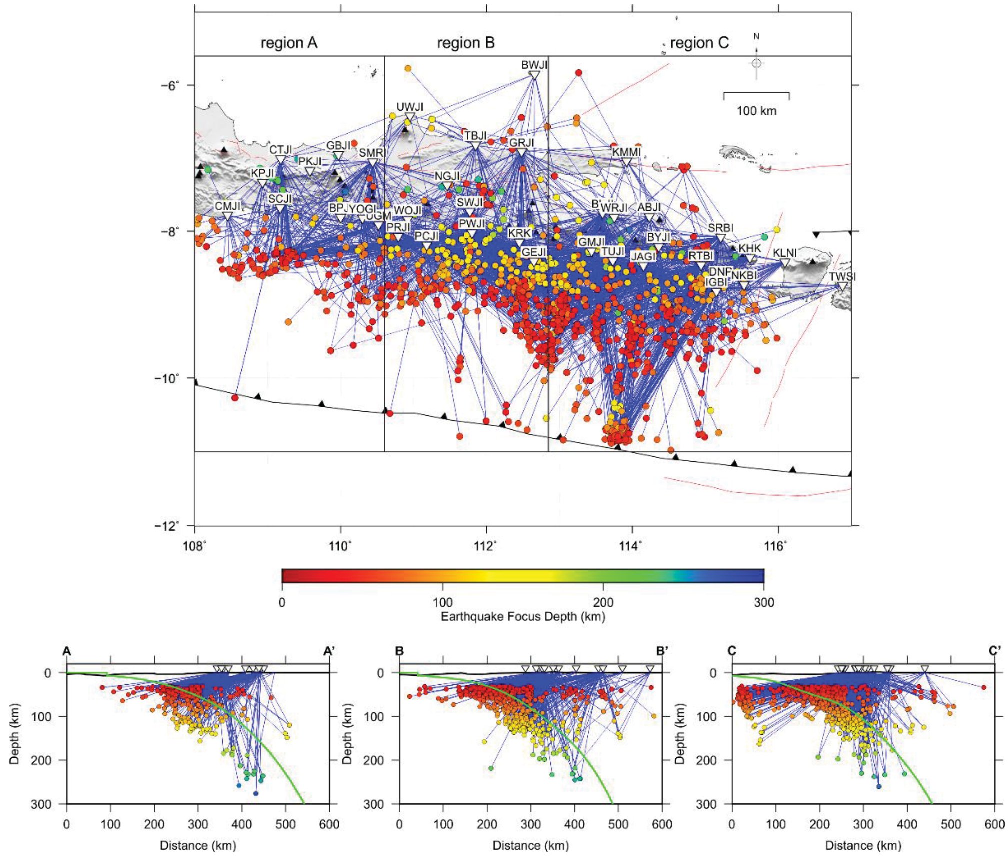

Figure V.2 Map of 38 BMKG stations (inverted triangles) and seismicity distribution used in this study from 2009 to 2020 (colored circles). The region of Central Java (A), western East Java (B), and easternmost East Java (C) are used to plot the vertical cross-sections below, and blue lines indicate straight-line ray path.

As done in the previous chapter, the series of selected seismograms were pre-conditioned in order to prevent program crashes in the splitting measurement, using the Obspy Toolbox on python (Beyreuther et al., 2010). The stage includes downsampling or trimming the seismogram to less than 10,000 samples, storing header variables (e.g. S-arrivals, event and station location, origin time, pick a grade, etc.) and converting the initial extension file (MSEED) to the SAC data triplets of E, N, Z component. As a result, we were finally able to perform an automatic shear wave splitting algorithm of the MFAST package (Savage et al., 2010) that adapts both the SC91 method (Silver and Chan, 1991) and cluster analysis method (Teanby et al., 2004).

V.2 Splitting Measurement

In the MFAST package, the processing stage starts from automatically performing a series of bandpass filters ranging from 0.4 to 10 Hz (Table IV.1), based on the signal-to-noise ratio (SNR) calculation for each earthquake-station pair. The SNR is defined as the average root mean square ratio of the signal and noise windows in the horizontal component of seismograms calculated from 3 s window after the S-pick. The filtered seismograms with SNR > 3 are then rotated into the SC91-determined incoming polarization direction (p) and its perpendicular value ($p^{\perp}$) on horizontal components. SC91 applies an inverse splitting operator, determined by a grid search over possible values (Silver and Chan, 1991). The inverse operator that removes the shear wave splitting gives the best resultant shear-wave splitting parameters. Contours of λ_2 for all the operators considered give a measure of confidence region by using an F-test (SC91).

The cluster analysis is implemented to find the stable solution with small errors over a given set of time windows to avoid the subjectivity in selecting the proper width of the time window that causes ambiguous splitting parameters (Teanby et al., 2004). It resulted in possible pairs of fast azimuths and delay times and clustered to a few stable regions of window space as we plot in the graph of ϕ vs δt. The cluster with the minimum variance is decided as the best cluster, and within that cluster, the measurement with the minimum variance is decided as the best measurement, and it is used as the final measurement for that phase at that filter (Savage et al., 2010). In advance of using the MFAST package, it also implements the grading criteria to evaluate quality measurement from A to D, based on the SNR, uncertainties and the stability of the clusters. We used the measurement with the grade of A and/or B (AB) to analyze the anisotropic structure beneath the study area. The criteria of AB measurements are: [1] SNR > 3, [2] $\delta t < 0.8 * tlag_{max}$ ($tlag_{max}$ is the maximum δt for grid search), [3] the maximum error of 25° for the polarization, and if the measurements have a A or B cluster grading in cluster analysis (Table IV.2) (Figure V.3 and V.4).

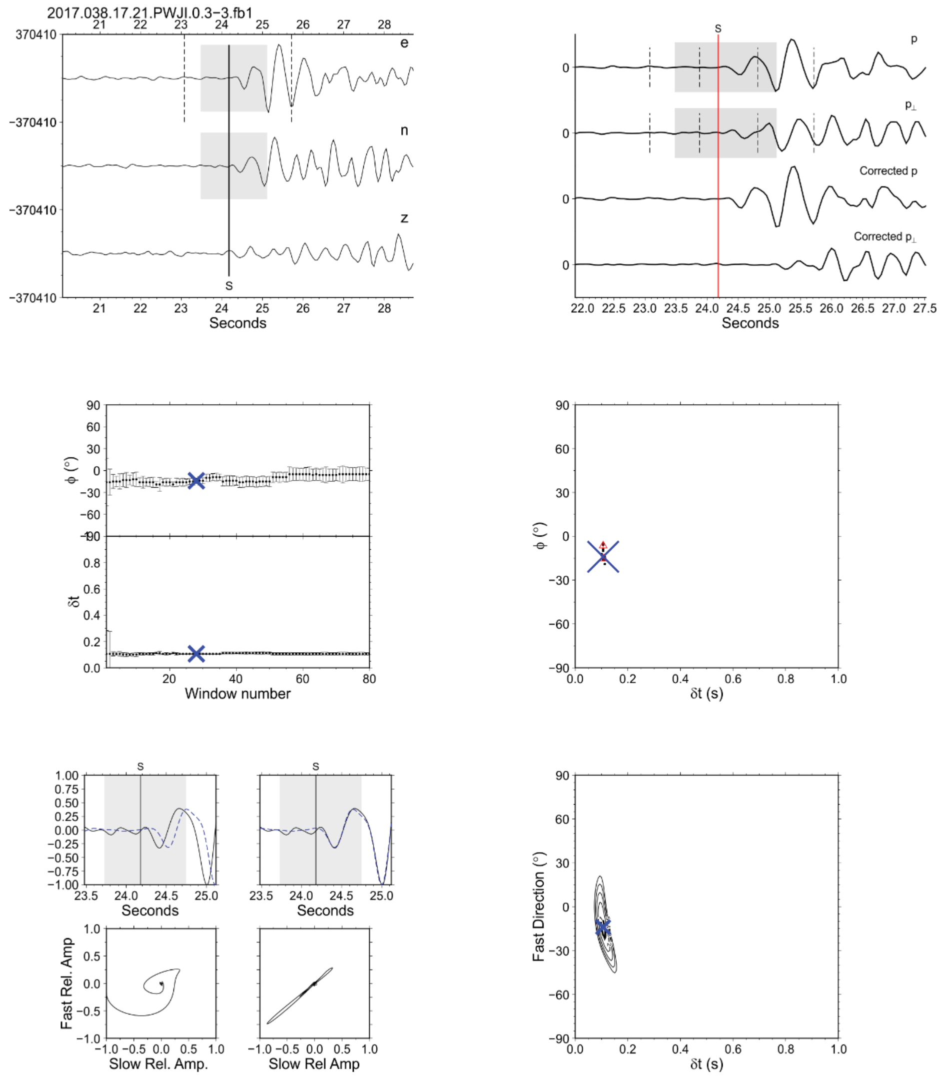

Figure V.3 High-quality, A-grade measurement recorded at PWJI station for 7 February 2017 event. The top-left panel shows the manual S-pick (black line) on three components (e, n, and z) of the seismogram. Dashed lines indicate the starting time and end time for the different S-wave analysis window. The top-right panel displays the rotated horizontal components before correction for splitting (p and $p^{\perp}$) and after the correction for splitting (corrected p and corrected $p^{\perp}$). Grey shaded areas in top figures indicate the selected S-wave analysis window. Two middle panels show the splitting parameters (best solution is marked by blue cross) obtained from the (Teanby et al., 2004) cluster analysis. The bottom-left panel indicates the particle motion plots before and after the correction for S-wave splitting. The bottom-right panel is the contours of the smallest eigenvalue of the covariance matrix for the final chosen SC91 measurement.

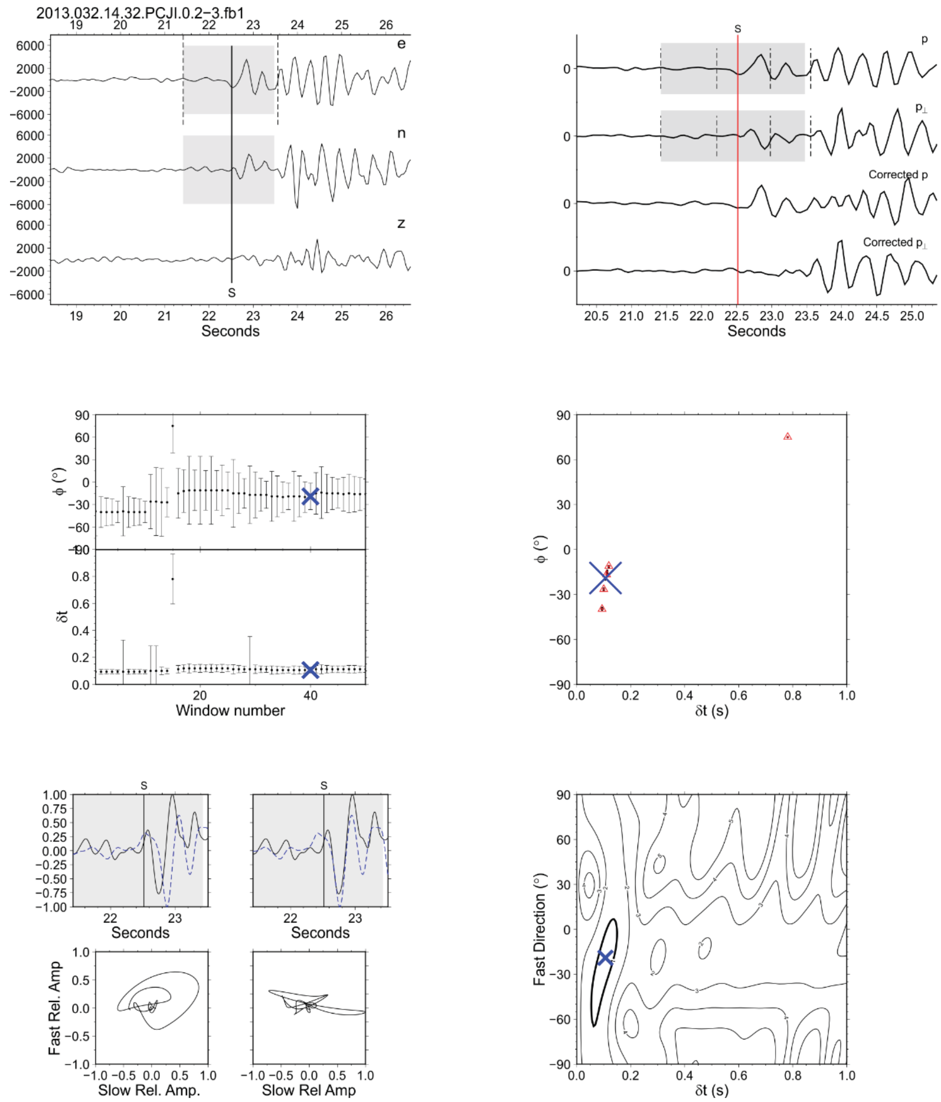

Figure V.4 Same as Figure V.3 but with a B grade measurement recorded at PCJI station for 1 February 2013 event.

V.3 2-D Delay Time Tomography and Spatial Averages

A heterogeneous anisotropic medium is observed using 2-D delay time tomography and a spatial averaging technique (TESSA) of Johnson et al. (2011). The code provides the first-order approximation of lateral variation in anisotropy. A δt from a single measurement is an estimation of anisostropic medium along the ray path from source to the station, and it is considered to be proportional to the path length of the ray (L) through the anisotropic medium (Silver, 1996). In TESSA, the total anisotropy observed along the ray path (δt_r) is the total of δt for each grid block (δt_b) with variable strength of anisotropy (S_b) in lateral direction (Johnson et al., 2011; Karalliyadda and Savage, 2013). The straight-line ray tracing that connects events to the station is divided into the lengths of ray segments on each grid block (L_{rb})., Thus, the total anisotropy can be determined by:

$$\delta t_r = \sum_{b=1}^{n} (S_b \times L_{rb}) \tag{V.1}$$

The code estimates the strength of anisotropy for each block (S_b) using a medium-scale optimization inversion function in MATLAB that finds the linear least-square solution of the problem, iteratively. It further converges to a final solution for the strength of anisotropy of the whole ray (S_r) within the boundary constraints. The minimum S_r will always be above 0 s/km and the maximum S_r will be less than $\delta t_{r(\max)}/L_b$, as the boundary constraints are applied. A $\delta t_{r(\max)}$ is the maximum delay time (δt) observed along a raypath and L_b is the grid size. A δt is assumed in the tomography method as simplification of a non-linear relationship between heterogeneous anisotropy and the observed apparent δt at the surface and does not accont for depth dependence of the anisotropy (Johnson et al., 2011; Savage et al., 2016)In this study, we used regular gridding with the size of 25 km and set the minimum number of rays to be 10 so if only a few rays are traveling through a box, the box will not be included in the calculation (Figure V.5).

We perform a checkerboard resolution test to evaluate which region can be resolved by the available dataset. The test starts from constructing the initial checkerboard model with given anisotropy strength values of 0.01 s/km and 0.02 s/km, then adding random noise generated from a standard normal distribution. Synthetic δt measurements are obtained and inverted using the method as previously described. Figure V.6 shows a result from the checkerboard resolution test. We use the tomographic weighting method to determine the average ϕ in the defined grid box. The method considers any variations due to the heterogenous anisotropic medium. The weighting function (ω_{rb}) is applied on the strength of anisotropy from each grid box (S_b) so the regions with higher strength of anisotropy will have more given a weighting. ω_{rb} is estimated from S_b along the raypath normalised by delay time for that raypath (δt_r).

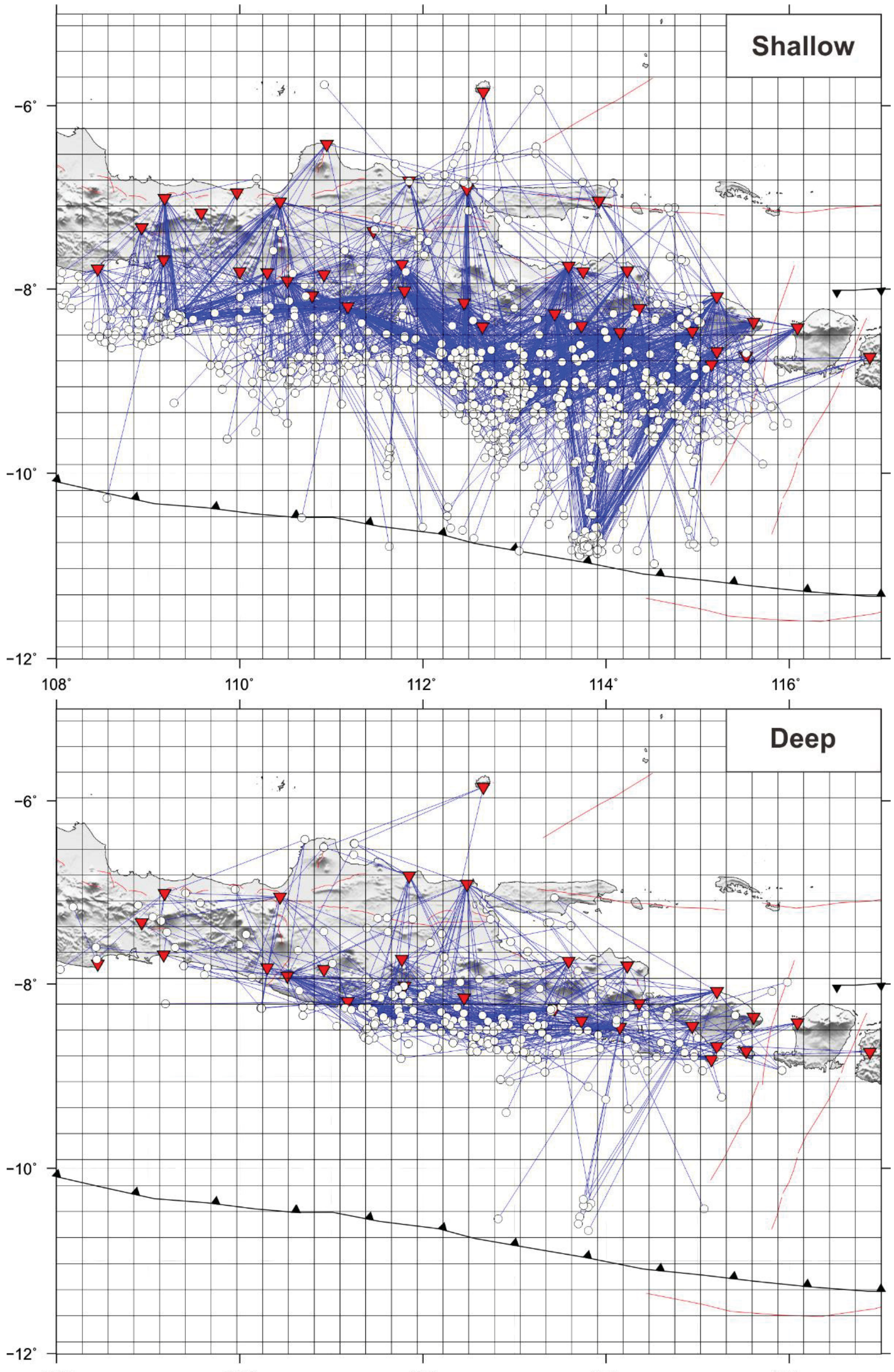

Figure V.5 Grid and ray path (blue lines) distribution used in the TESSA inversion for events below and above 100 km depth. White circles and red inverted triangles are epicenters and stations, respectively.

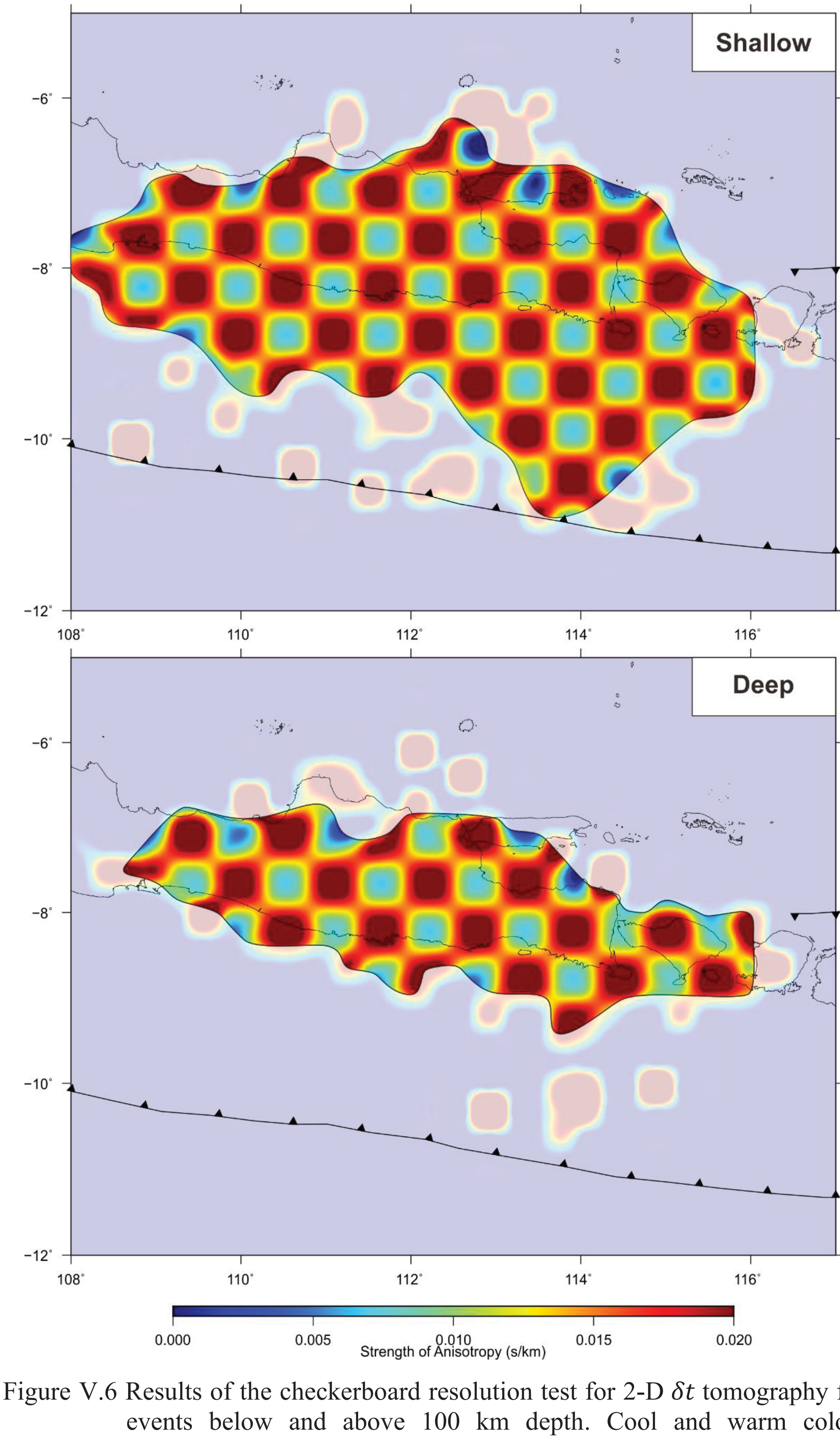

Figure V.6 Results of the checkerboard resolution test for 2-D δt tomography for events below and above 100 km depth. Cool and warm colors represent weak and strong anisotropy, respectively.

V.4 Results

A total of 2,375 local S-splitting measurements were obtained from 38 BMKG stations at focal depths between 30-300 km with various delay times (δt) and anisotropy orientation (ϕ) (Figure V.7). We divide the anisotropic analysis into two depth units: shallow (≤100 km) and deep (>100 km) based on the lithospheric-asthenosphere boundary beneath the Java region, which shows a lithosphere thickness of ~100 km (Hamza and Vieira, 2012). The normalized circular histograms (rose diagrams) of fast polarizations (ϕ) at each station are plotted in Appendix E. These histograms represent high quality result of AB grade measurements from single earthquake-station pair. Tables V.1, V.2, and V.3 summarize the average splitting parameters at each station using all depths, shallow and deep earthquakes, respectively.

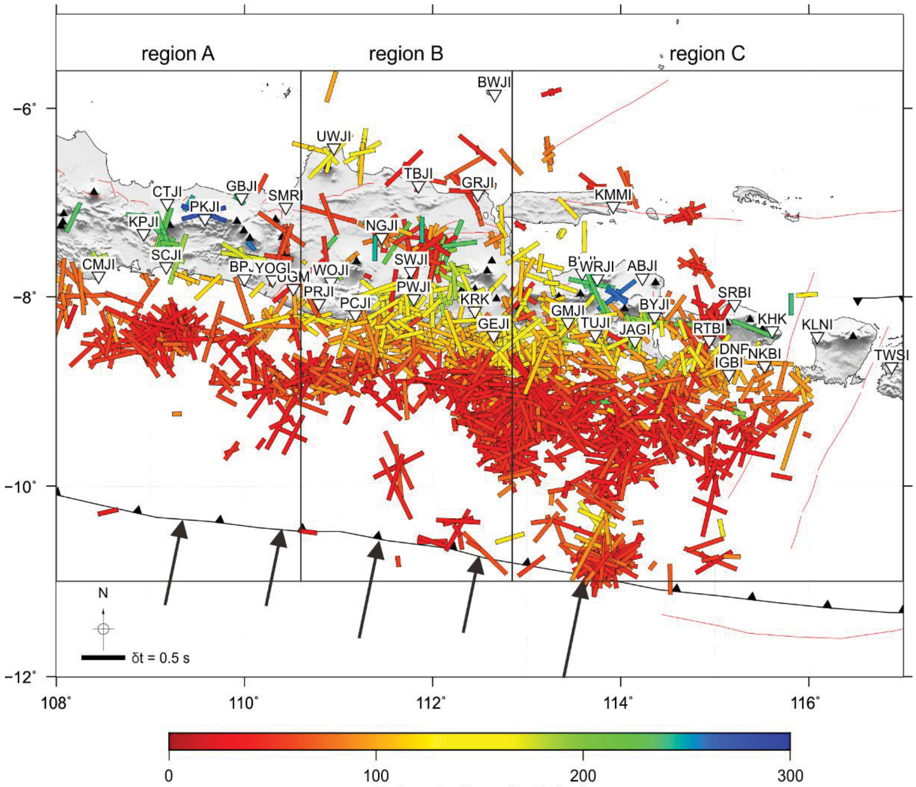

Figure V.7 Local S-wave splitting results beneath Central and East Java region. Bars orientated in the direction of the fast shear wave polarizations (ϕ), the length of the bar is proportional to the delay times (δt), and the color of the bar represents earthquake focus depth (km) for each measurement. Black arrows are Indo-Australian plate motion direction relative to the Eurasian plate based on GPS observations (Koulali et al., 2017).

We implement directional statistics of Mardia (1972) and Gerst and Savage (2004) to calculate the uncertainties (e.g. mean, standard deviation (SD), standard error (SE)) of the single station splitting measurements. Since the ϕ has a bimodal distribution (180° ambiguity), directional statistics provide quantitative estimation of the mean ϕ and the errors using different calculation from normal statistics. We also estimate R, which is a quantitative estimation of circular spread from the mean angular azimuth (ϕ). SE of ϕ is calculated using R and the concentration parameter (κ), which is a parameter of Von Mises distribution $V\ M_{(\phi,\kappa)}$. Tables V.1, V.2, and V.3 summarize the average splitting parameters of each station and its statistical parameters i.e. mean, standard deviation (SD), standard error (SE) for all depths, shallow and deep earthquakes, respectively.

Table V.1 Average results of splitting parameters using the number of all depth earthquakes (N) at each station. Mean ϕ : mean fast azimuth, SE: standard error, CSD: circular standard deviation, R: mean resultant vector of ϕ, mean δt: mean delay time, SD: standard deviation

STA	N	Mean ϕ	SE of ϕ	CSD of ϕ	R	Mean δt	SE of δt	SD of δt
ABJI	52	-3.08	13.87	51.36	0.20	0.34	0.03	0.19
BLJI	106	1.58	21.63	62.76	0.09	0.30	0.02	0.18
BPJI	7	44.78	23.34	43.29	0.32	0.31	0.05	0.14
BWJI	8	-48.08	17.48	39.16	0.39	0.22	0.05	0.14
BYJI	73	-53.53	15.65	55.74	0.15	0.35	0.03	0.21
CMJI	25	-84.80	98.04	72.32	0.04	0.27	0.04	0.22
CTJI	46	18.66	13.91	50.44	0.21	0.35	0.03	0.18
DNP	76	80.89	11.01	50.72	0.21	0.36	0.02	0.21
GBJI	5	83.74	22.38	39.39	0.39	0.51	0.05	0.12
GEJI	4	-79.50	232.31	71.71	0.04	0.31	0.11	0.22
GMJI	220	-57.99	17.97	65.06	0.08	0.27	0.01	0.18
GRJI	74	51.69	53.69	71.65	0.04	0.28	0.02	0.20
IGBI	74	67.31	11.88	51.70	0.20	0.33	0.02	0.18
JAGI	284	77.10	8.13	56.09	0.15	0.28	0.01	0.19
KHK	33	10.07	14.67	48.62	0.24	0.33	0.04	0.20
KLNI	28	-6.33	26.46	56.41	0.14	0.30	0.04	0.19
KMMI	14	-20.95	7.80	28.33	0.61	0.36	0.04	0.15
KPJI	15	83.28	20.37	47.53	0.25	0.39	0.05	0.18
KRK	100	-86.62	18.15	60.04	0.11	0.35	0.02	0.20
NGJI	6	51.79	52.06	55.05	0.16	0.48	0.09	0.21
NKBI	11	-40.53	11.52	34.04	0.49	0.23	0.05	0.18

PCJI	203	87.57	14.46	61.73	0.10	0.27	0.01	0.20
PKJI	4	-60.44	11.42	23.02	0.72	0.40	0.13	0.26
PRJI	6	-65.70	17.95	36.89	0.44	0.35	0.08	0.21
PWJI	198	-87.42	19.82	65.62	0.07	0.24	0.01	0.16
RTBI	114	-10.42	16.65	59.75	0.11	0.33	0.02	0.20
SCJI	34	25.18	60.95	68.58	0.06	0.32	0.04	0.21
SMRI	67	-83.56	14.02	53.47	0.18	0.32	0.03	0.21
SRBI	107	-35.33	9.74	51.47	0.20	0.33	0.02	0.20
SWJI	105	-68.68	13.20	55.91	0.15	0.31	0.02	0.18
TBJI	38	31.25	17.22	52.28	0.19	0.38	0.03	0.18
TUJI	11	80.73	13.04	36.55	0.44	0.25	0.05	0.17
TWSI	9	-47.25	28.05	48.59	0.24	0.25	0.04	0.13
UGM	154	-73.92	13.41	58.84	0.12	0.31	0.02	0.19
UWJI	8	-12.56	23.60	44.67	0.30	0.33	0.07	0.20
WOJI	8	-65.29	13.62	34.22	0.49	0.36	0.08	0.23
WRJI	5	54.02	29.24	44.31	0.30	0.29	0.10	0.22
YOGI	43	89.87	12.34	47.94	0.25	0.23	0.02	0.15

Table V.2 Same as Table V.1 for the shallow earthquakes (<100 km depth)

STA	**N**	**Mean ϕ**	**SE of ϕ**	**CSD of ϕ**	**R**	**Mean δt**	**SE of δt**	**SD of δt**
ABJI	38	-0.58	26.72	58.70	0.12	0.35	0.03	0.21
BLJI	82	-13.08	25.49	63.22	0.09	0.30	0.02	0.19
BPJI	6	43.61	14.07	31.89	0.54	0.29	0.06	0.15
BWJI	5	-43.20	6.25	14.04	0.89	0.15	0.03	0.06
BYJI	59	-57.18	12.74	51.01	0.20	0.36	0.03	0.22
CMJI	20	-70.40	21.09	50.44	0.21	0.26	0.05	0.23
CTJI	38	20.77	16.43	51.56	0.20	0.33	0.03	0.18
DNP	72	82.10	9.31	47.55	0.25	0.36	0.02	0.21
GBJI	3	-67.82	21.07	33.10	0.51	0.56	0.08	0.13
GEJI	3	58.00	34.07	42.46	0.33	0.19	0.07	0.12
GMJI	165	-56.94	17.29	62.72	0.09	0.27	0.01	0.17
GRJI	45	33.35	17.49	53.81	0.17	0.27	0.03	0.21
IGBI	61	69.53	10.02	47.39	0.25	0.33	0.02	0.19
JAGI	217	81.39	8.50	54.78	0.16	0.27	0.01	0.19
KHK	29	17.18	22.60	54.36	0.17	0.33	0.04	0.20
KLNI	23	-22.05	25.89	54.65	0.16	0.30	0.04	0.20
KMMI	13	-17.80	7.79	27.51	0.63	0.34	0.04	0.14
KPJI	13	69.25	20.02	46.02	0.28	0.41	0.05	0.18
KRK	73	-89.11	42.58	68.86	0.06	0.34	0.02	0.20
NGJI	5	83.25	46.32	51.91	0.19	0.45	0.10	0.22
NKBI	7	-46.78	11.13	28.53	0.61	0.18	0.04	0.11
PCJI	145	76.12	14.56	59.56	0.12	0.28	0.02	0.21

PKJI	4	-60.44	11.42	23.02	0.72	0.40	0.13	0.26
PRJI	4	-47.17	10.33	20.93	0.77	0.39	0.09	0.18
PWJI	159	-76.95	50.22	75.17	0.03	0.24	0.01	0.16
RTBI	92	-2.65	22.20	62.17	0.09	0.34	0.02	0.21
SCJI	27	2.86	26.51	56.17	0.15	0.33	0.04	0.22
SMRI	54	-75.32	19.81	56.97	0.14	0.32	0.03	0.22
SRBI	87	-36.11	13.63	55.01	0.16	0.32	0.02	0.20
SWJI	83	-70.47	13.32	54.31	0.17	0.31	0.02	0.18
TBJI	23	43.46	56.04	65.16	0.08	0.34	0.03	0.16
TUJI	6	83.19	9.27	22.89	0.73	0.25	0.07	0.17
TWSI	7	-43.54	26.65	45.62	0.28	0.25	0.05	0.14
UGM	109	-80.97	30.77	67.36	0.06	0.32	0.02	0.18
UWJI	8	-12.56	23.60	44.67	0.30	0.33	0.07	0.20
WOJI	4	-36.13	13.37	26.43	0.65	0.36	0.11	0.23
WRJI	3	52.07	45.01	47.33	0.26	0.20	0.06	0.10
YOGI	34	-83.64	16.82	51.05	0.20	0.22	0.02	0.14

Table V.3 Same as Table V.1 for the deep earthquakes (>100 km depth)

STA	N	Mean ϕ	SE of ϕ	CSD of ϕ	R	Mean δt	SE of δt	SD of δt
ABJI	13	-4.69	14.66	40.43	0.37	0.32	0.03	0.11
BLJI	22	19.57	19.31	49.79	0.22	0.29	0.03	0.12
BWJI	3	57.68	22.80	34.72	0.48	0.34	0.09	0.15
BYJI	14	7.87	41.22	57.78	0.13	0.32	0.05	0.19
CMJI	2	-4.50	25.69	33.00	0.52	0.28	0.06	0.09
CTJI	8	11.75	24.10	45.03	0.29	0.40	0.06	0.16
DNP	4	0.19	14.95	28.85	0.60	0.44	0.08	0.16
GMJI	55	-67.04	84.67	75.08	0.03	0.26	0.03	0.19
GRJI	26	-54.79	20.54	52.08	0.19	0.26	0.03	0.17
IGBI	13	2.97	47.30	59.18	0.12	0.29	0.04	0.13
JAGI	64	59.91	20.28	58.49	0.12	0.31	0.02	0.20
KHK	4	-0.11	8.23	16.61	0.85	0.36	0.10	0.19
KLNI	5	26.86	20.30	37.52	0.42	0.32	0.07	0.16
KPJI	2	-62.00	9.32	13.23	0.90	0.23	0.04	0.05
KRK	27	-85.20	14.59	46.86	0.26	0.37	0.03	0.18
NKBI	2	-87.50	47.91	44.93	0.29	0.14	0.07	0.09
PCJI	56	-71.12	17.17	55.16	0.16	0.24	0.02	0.17
PWJI	39	87.22	12.72	47.64	0.25	0.24	0.02	0.14
RTBI	22	-24.06	18.35	48.96	0.23	0.29	0.04	0.18
SCJI	4	71.66	10.86	21.95	0.75	0.30	0.07	0.14
SMRI	13	83.99	13.94	39.47	0.39	0.30	0.04	0.16
SRBI	20	-33.90	11.55	39.99	0.38	0.36	0.05	0.22
SWJI	21	-43.17	60.98	65.65	0.07	0.28	0.04	0.19

TBJI	14	31.91	14.46	40.87	0.36	0.43	0.05	0.18
TWSI	2	-74.50	91.00	55.18	0.16	0.26	0.03	0.04
TUJI	4	82.19	27.45	41.14	0.36	0.17	0.03	0.05
WOJI	2	-77.00	13.81	19.78	0.79	0.14	0.01	0.01
UGM	41	-74.64	13.78	49.36	0.23	0.28	0.03	0.19
YOGI	8	79.68	17.50	39.18	0.39	0.25	0.07	0.19

In general, the average fast directions are parallel, sub-parallel, and perpendicular relative to the trench for all depth events. The trench-parallel fast directions (E-W orientation) can be observed at some stations in southern Java (e.g., CMJI, KPJI, YOGI, UGM, PCJI, PWJI, KRK, GEJI, TUJI, JAGI). Meanwhile, considerable variations in fast direction are shown at some stations with two distinct trench sub-parallel fast directions i.e., NE-SW (e.g. CTJI, SCJI, BPJI, NGJI, TBJI, GRJI, WRJI, IGBI) and NW-SE orientation (e.g. PKJI, PRJI, WOJI, UWJI, SWJI, GMJI, BYJI, KMMI, SRBI), and also trench-perpendicular fast directions (N-S) (e.g. BLJI, ABJI, RTBI, KHK, KLNI) that are mostly situated in the eastern region. At most stations, δt-s are within the range of 0.16-0.38 s, but some stations have exceptionally high δt (> 0.4 s) i.e., GBJI, NGJI, PKJI.

Since the earthquakes are mostly located at < 100 km depth, the splitting pattern obtained from shallow earthquakes is also considerably similar to the fast directions using all depth events. It indicates that the shallow anisotropic medium probably becomes a major influence on the observed fast directions at most stations. The dissimilar pattern can be observed at some stations e.g., SCJI, GBJI, NGJI, GEJI, BLJI, KLNI which have fewer splitting measurements than other stations. The average δt-s for the single station is also within 0.16-0.38 s and exceptional high δt (> 0.4 s) at GBJI, NGJI, PKJI stations. In contrast, the average fast directions obtained from deeper earthquakes (100 – 300 km depths) show changes in splitting orientation. They exhibit trench-perpendicular or N-S orientations at most stations located in Central Java (region A) and easternmost Java and Bali (region C) with δt of 0.23 – 0.44 s, while the trench-parallel fast directions are observed in the western East Java region (region B) with δt of 0.14 – 0.37 s.

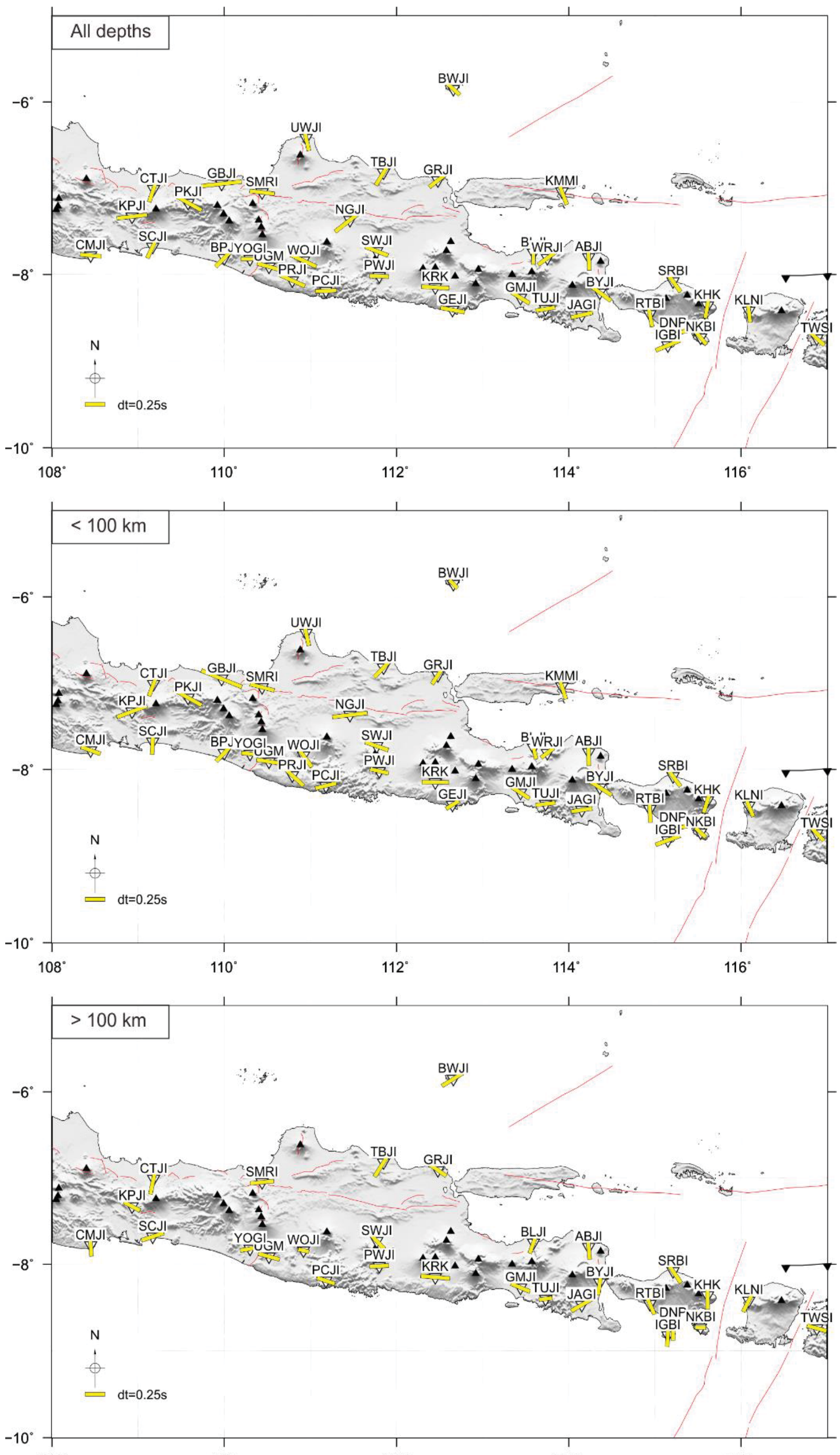

Figure V.8 The average splitting parameters at each station using all depths, shallow and deep earthquakes, respectively. Bars are orientated in the direction of the fast shear wave polarizations (ϕ), and the length of the bar is proportional to the delay times (δt).

Splitting measurements along the ray path in the lithosphere can contribute to the total anisotropy in a given region, using S-waves of local and regional events. Thus, it is associated with the different sources of anisotropy developed by shape preferred orientation (SPO) and lattice preferred orientation (LPO). In most subduction zones, the average fast polarizations show both parallel and perpendicular to the direction of plate motion (Collings, 2012). If the seismic anisotropy at mantle depths occurs through a simple LPO mechanism, the fast axis of olivine, a predominant mantle mineral, is parallel with the maximum shear direction. Thus, the fast directions of the S-wave tend to align with the plate motion (Long, 2013). On the other hand, the olivine fabric can be deformed due to the high-stress condition and water content, resulting in the axis of olivine aligning perpendicular to the plate motion. Furthermore, the SPO mechanism is still possible due to the anisotropy caused by structure in the upper layer (e.g. Fischer et al., 2000).

V.5 Discussion

V.5.1 Spatial and Vertical Variations of Splitting Parameters

Spatial variation of splitting parameters shown in Figure V.7 and V.8 indicates the complex anisotropic features beneath the Central and East Java region. However, we suggest that the pattern in fast direction is generally trench-parallel measured at stations located close to the trench in the forearc region, while the transition zone from trench-parallel to trench-perpendicular ϕ at stations located further from the trench. A similar pattern is also observed in several subduction settings with various locations of the transition zone e.g., northeastern Japan (Long and van der Hilst, 2006; Nakajima and Hasegawa, 2004) and Tonga (Smith et al., 2001) that the transition occurs at the arc and further backarc, respectively. In comparison, Hammond et al. (2010) conducted the local S and SKS splitting measurements around the Java-Sumatra subduction zone using a fewer number of stations. They observed trench-parallel ϕ from shallow and deep earthquakes, while the trench-perpendicular ϕ are observed from the intermediate depth earthquakes (250-350 km). The δt-s from earthquakes < 300 km depth are within 0.06 – 0.72 s (with an average of 0.36 s) at UGM station. Our measurements at

UGM station yield the average δt of 0.19 s that are still in the range of their estimation.

According to the ray geometry, seismic anisotropy sampled by most of the stations is coming from slab earthquakes and mainly propagate in the mantle wedge to the seismic stations on the surface. Therefore, mantle wedge may contribute most of the anisotropy for the observed shear-wave splitting. A rule of thumb to interpret the pattern of fast directions in the upper mantle has been carried out since early deformation experiments of Zhang and Karato (1995) that the fast directions generally indicate the direction of horizontal mantle flow beneath the seismic stations. It is commonly due to the lattice preferred orientation of olivine fabrics. For A-type olivine fabric, which presents at the region with relatively low stresses, high temperatures, and low water contents (Karato et al., 2008), will develop an LPO mechanism in which the fast axes of olivine crystals tend to align with the shear direction and flow directions as geodynamical consequences. The N-S orientation or trench-perpendicular of fast directions in the northern region may reflect the 2-D mantle flow since they are orientated parallel with the relative plate motion (Koulali et al., 2017). Di Leo (2012) inferred several types of flows in the upper mantle beneath the Indonesia region, one of which is trench-perpendicular flow in the Sumatran backarc as also observed in Java since the regions are in the same subduction system. The discussion about whether mantle flow in the subduction zone is either trench-perpendicular or -parallel may be oversimplified despite more complex flow at the convergent plate (Di Leo et al., 2012). However, in most observations in regions of oceanic lithosphere, the seismic anisotropy suggests mantle flow direction be well correlated with the plate motions (e.g., Becker, 2008; Becker et al., 2003; Conrad et al., 2007; Kreemer, 2009).

Several factors can affect the geometry of olivine fabric e.g., water content, stress, temperature, presence of melt, etc. Therefore, the subduction zone anisotropy may exhibit a more complex pattern in fast directions that is not expected as the rule of thumb. Jung and Karato (Jung and Karato, 2001) demonstrated the development of B-type olivine fabric from water-saturated samples deformed in simple shear. Low temperature, high stress, and high-water content are playing important roles in developing B-type olivine fabrics which have been found in natural peridotite rocks (Karato et al., 2008) as the Java subduction may meet this condition. The average of fast directions in the southern region shows predominant trench-parallel orientation or perpendicular relative to the plate motion. It is consistent with the previous shear wave splitting studies in the Java-Sumatra subduction zone (i.e. Di Leo et al., 2012; Hammond et al., 2010), showing that local S-wave splitting results are predominant trench parallel obtained from < 300 km depth events. The Indo-Australian plate has been subducting below the Eurasian plate since ~45 Ma (Hall, 2002), providing low temperature on the subducted slab to support the high-pressure environment. A large formation of hydrous minerals is concentrated in the shallow part of the subducting slab that is hydrated through the lithospheric deformation, hydrothermal circulation, and faulting at the outer rise (e.g., Johnson and Pruis, 2003; Ranero et al., 2003). These minerals become unstable when the pressures and temperatures are high, water is released into the wedge (Cagnioncle et al., 2007), promoting partial melting and serpentinizing the mantle wedge.

In addition, Jung and Karato (2001) suggest that the presence of water in the mantle can make B-axis olivine tend to align with the flow direction, resulting in the fast directions of the shear wave being orientated perpendicular to the direction of mantle flow. Based on the tomographic study in the previous chapter, the low-velocity anomalies (Vp and Vs) with high Vp/Vs ratio (>1.75) dominate around the volcanic complex, which may reflect some features such as sediments, fluids, or thermal structure derived from the subducted slab. These features may affect the fast directions of the shear wave observed at surrounding stations.

Another possible mechanism of anisotropy in the mantle is due to the shape preferred orientation (SPO) of the partial melting. A study by Fischer et al. (2000) demonstrated that melt-filled inclusions could produce perpendicular-fast polarization to the direction of plate motion. The previous tomographic study observed the presence of partial melt beneath Central and East Java at about ~100 km depth indicated by low-velocity anomalies with a high Vp/Vs ratio. Therefore, this anisotropic mechanism only occurs at limited stations since the ascended melts are concentrated at certain regions beneath the volcanic complex.

We carried out the further analysis with respect to depth as presented in Figure V.9, V.10, and V.11, showing the vertical sections of fast directions across the region of Central Java (A), western East Java (B), and easternmost East Java (C), respectively. Stations that sample these regions with a considerable number of measurements reveal changes in fast directions (ϕ) with depth, e.g., SMRI in Figure V.9, PCJI, GRJI in Figure V.10, and RTBI, BLJI in Figure V.11. The splitting pattern is consistent with the previous anisotropy conducted by Hammond et al., (2010) using local S-splitting measurements that exhibit trench-parallel from shallow earthquakes and trench-perpendicular from intermediate earthquakes (250-350 km), in general. We also plotted the variations of δt with hypocentral distance for representative station in these three regions i.e. UGM, PCJI, JAGI (Figure V.12). The least square fitting indicates an increase in δt with length of ray path from sources to the stations. The relationship between these parameters (δt and ray path length) can be used to calculate the percentage of anisotropy (Savage, 1999) using the average shear wave velocity (Vs) model of Muttaqy et al. (2021 in review) and the highest grade of splitting measurements (A grade). Our calculations yield an average of 0.825, 0.865, and 0.729 % shear wave velocity anisotropy for regions A, B, and C, respectively (Figure V.12). If splitting parameters are affected by the structure above the slab, the anisotropy is probably due to the preferred orientation of highly anisotropic hydrous minerals (serpentine, talc) that formed along steeply dipping faults (Faccenda et al., 2008). In addition, fossilized anisotropy could occur in the lithospheric slab, as Hammond et al. (2010) suggested. As oceanic lithosphere is formed and moves over the asthenosphere, it accumulates a large anisotropic signature. According to Lithgow-Bertelloni and Richards (1998), the oceanic lithosphere subducting beneath Java formed in 80-140 Ma. The Australian plate moves eastward between 74-119 Ma, resulting in east-west anisotropy orientations at >100 km depth.

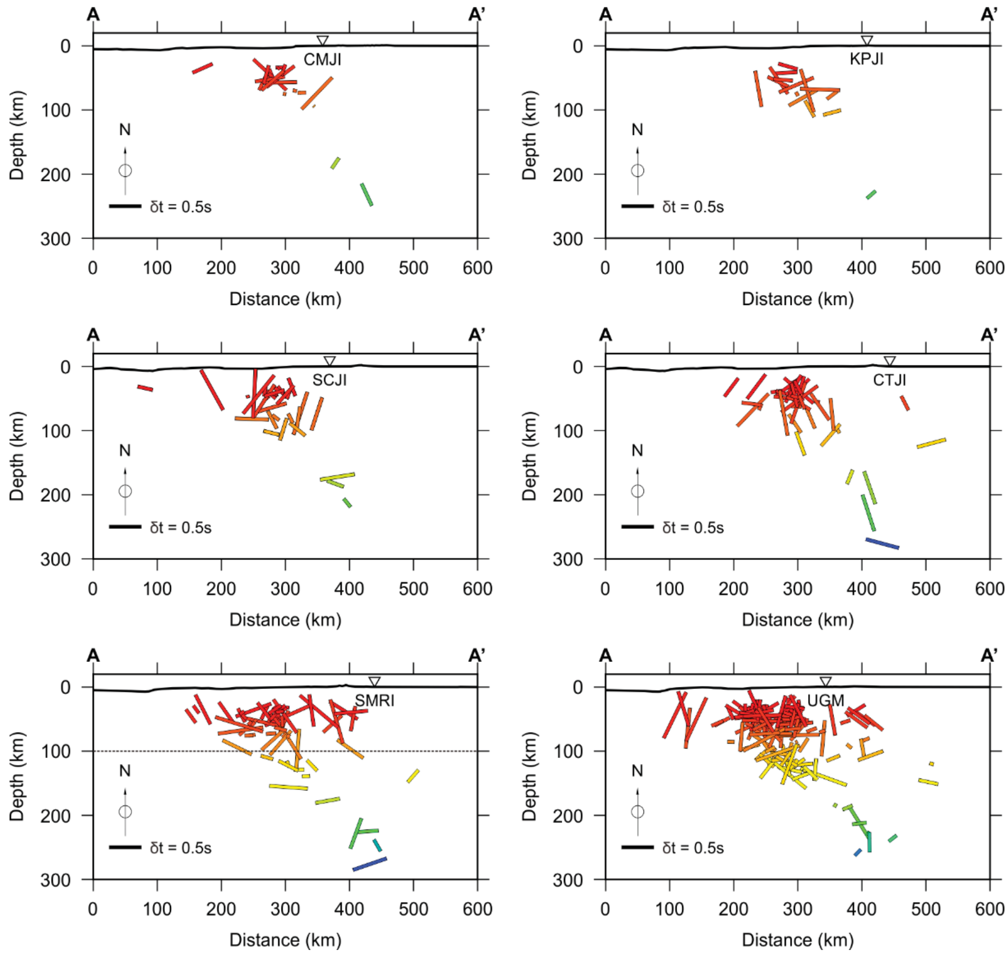

Figure V.9 Change of splitting parameters with depth in Central Java along the profile AA’ in Figure V.7. Station measurements displayed in the upper, middle, and bottom diagrams are located in the western, central, and eastern regions. The bars are orientated as in the horizontal plane, thus plotted relative to N as marked on the figure, and the length of the bar is proportional to the delay times (δt). The black dashed line indicates the visible change in fast azimuth (ϕ).

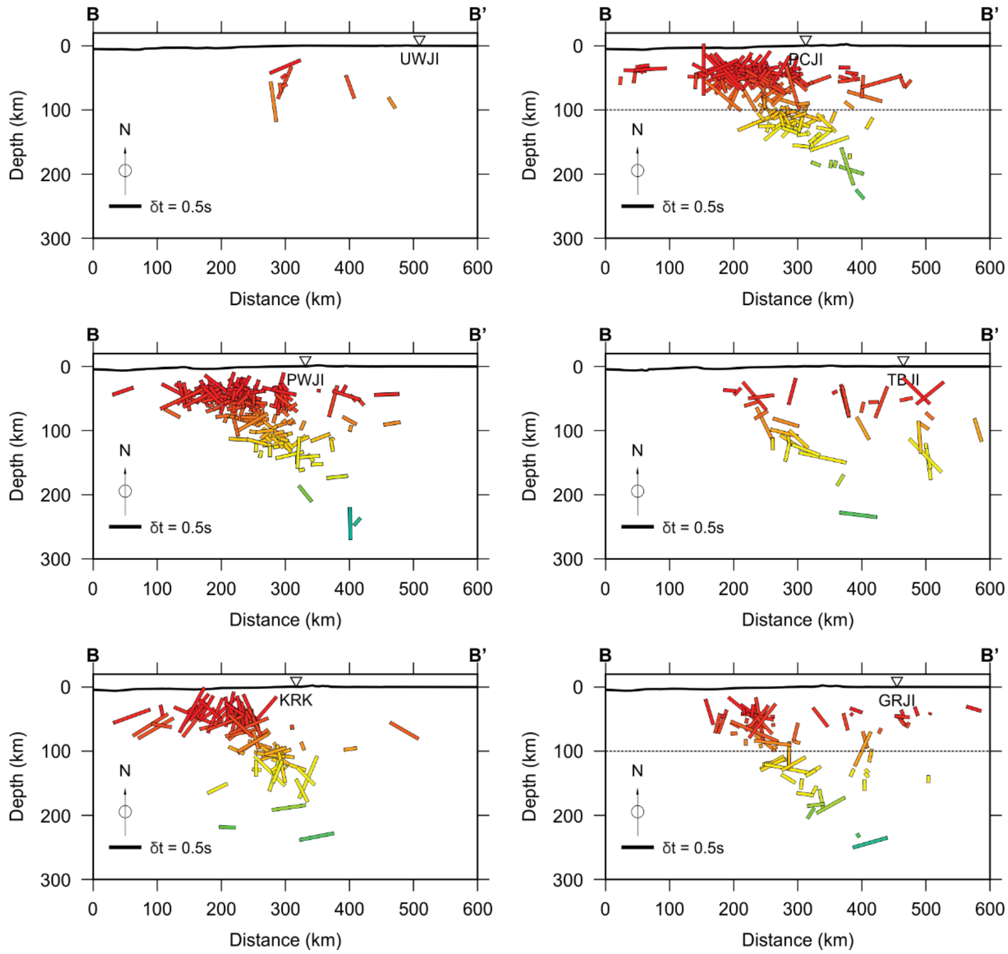

Figure V.10 Same as Figure V.9 but for the change of splitting parameters with depth in western East Java along the profile BB' in Figure V.7.

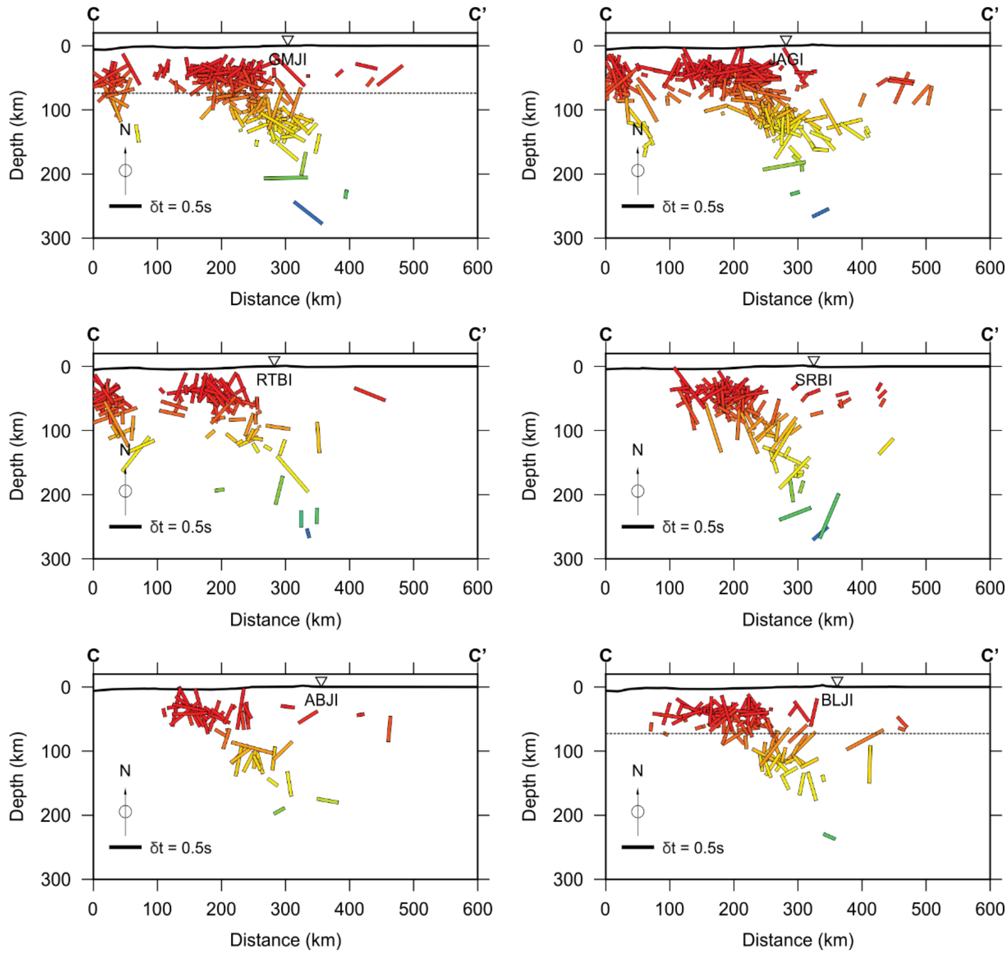

Figure V.11 Same as Figure V.9 but for the change of splitting parameters with depth in easternmost East Java along the profile CC' in Figure V.7.

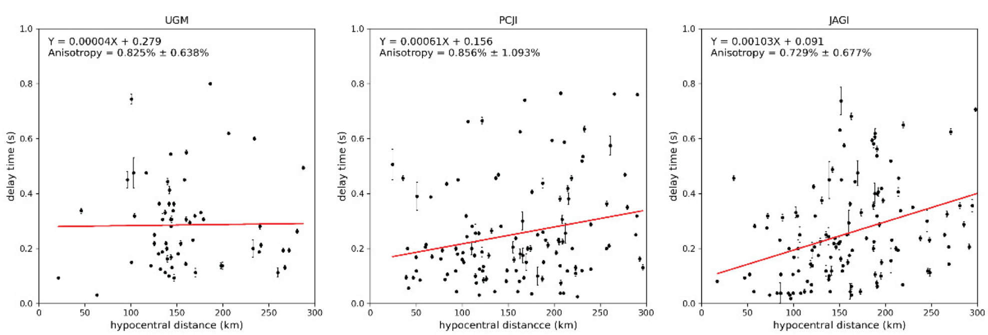

Figure V.12 Example of stations located in regions A, B, and C that shows changes in δt with hypocentral distance. The Red line indicates the least-squares fit of the data.

V.5.2 Interpretations from 2-D Delay Tomography and Spatial Averages

Figure V.8 exhibits an inconsistent pattern of splitting results at some closely spaced stations suggesting the occurrence of lateral variations in anisotropy. Thus, the maps of 2-D delay time tomography and the spatial average of fast direction may provide the average anisotropic structure around the region. Figure V.13 illustrates the 2-D distribution maps of δt for shallow (≤ 100 km) and deep (> 100 km) earthquake groups overlayed by the weighted average of ϕ at each grid block. These results are obtained using AB quality splitting parameters from 2,336 event-station pairs. The variation of anisotropy strength (s/km) is indicated by warm (yellow to red) and blue colors for the region with high (> 0.001 s/km) and low (≤ ~0.0075) anisotropy, respectively. The shaded region is a low resolution and/or large residuals region based on the checkerboard resolution test.

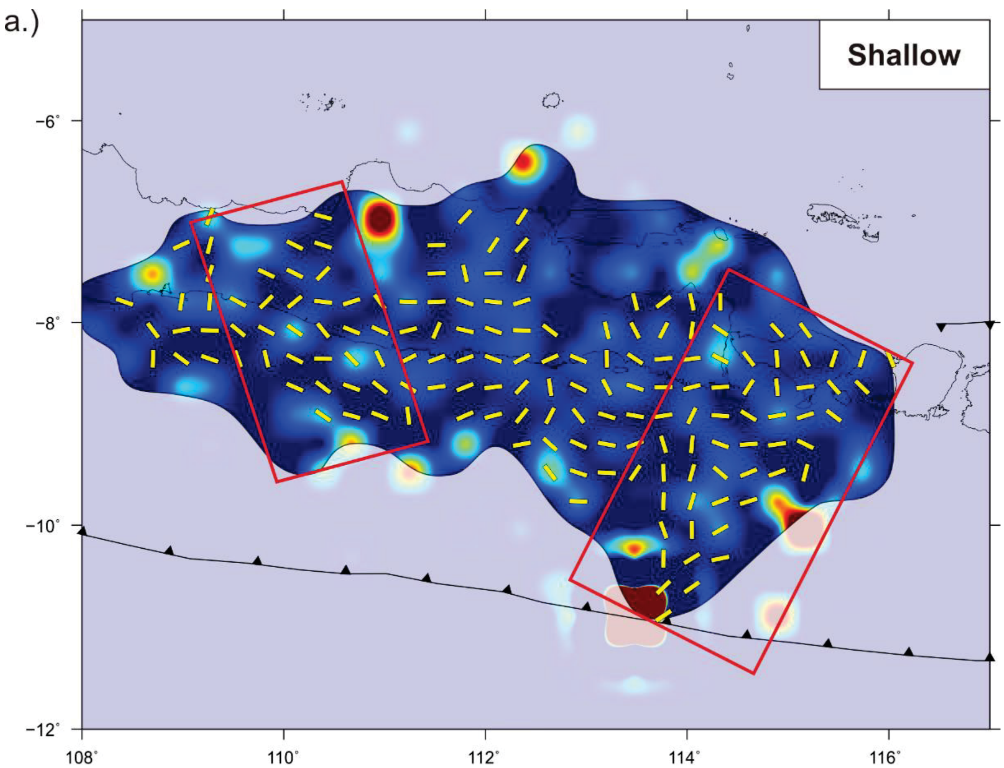

Figure V.13 Maps of 2-D delay time tomography and spatial averages from TESSA (Johnson et al., 2011) showing the distribution of splitting parameters for (a) shallow (≤ 100 km) and (b) deep (> 100 km) earthquakes. Warm (red to yellowish-green) and blue colors depict high and low strength of anisotropy. Yellow bars indicate the spatial averages of ϕ and the shaded region shows the regions with low resolution and/or large residuals.

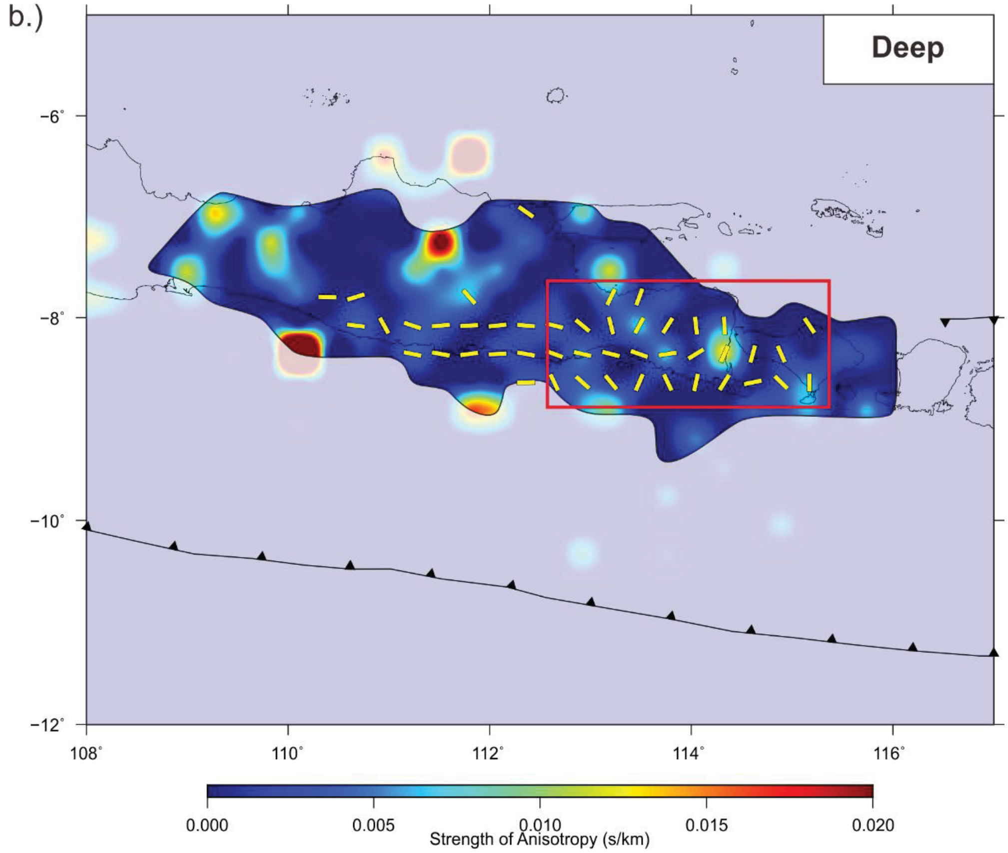

Figure V.13 (continued)

Overall, the Central and East Java region has relatively low to moderate strength of anisotropy with exceptionally high strength of anisotropy (> 0.015 s/km) at the region near subducted seamount that is responsible for the 1994 Java earthquake. The seamount modulates the seafloor bathymetry (Xia et al., 2021) and is manifested in the isolated free-air gravity anomaly close to the trench (Sandwell et al., 2014). Our tomographic results also indicate this feature as a low-velocity anomaly at the boundary of the subducted slab (~ 50 km depth) with a ~50 km width and extend to the depth of ~25 km. Interaction between subducting seamount and overriding plate suggests combination stress and structural effect to the anisotropy with the SPO mechanism. Faults and fractures created by subduction seamount are the hosts of migrating fluids, from over-pressured sediments downdip of the seamount, resulting in a complicated environment of stress distribution (Zal et al., 2020).

The tomographic weighted ϕ is obtained for each grid block that has a high density of seismic rays and spatial averages are not well constrained at some locations with a low density of rays (see Figure V.5 and V.13). Spatial averages of ϕ display consistent regional patterns which are predominant trench-parallel or perpendicular relative to the plate motion. Considerable variations in ϕ are shown at regions marked by red squares in Figure V.13 with distinct trench-subparallel to perpendicular orientations i.e. relative NW-SE at the western region and N-S to relative NE-SW at the eastern region observed from either shallow and deep earthquakes. As previously discussed, the trench-perpendicular or sub-parallel pattern suggests mantle flow direction that is usually well correlated with the plate motions (e.g., Becker, 2008; Becker et al., 2003; Conrad et al., 2007; Kreemer, 2009). It is caused by the simple lattice preferred orientation (LPO) mechanism coming from mantle material, developing A-type olivine fabric tends to align with the maximum shear direction (Long, 2013). Meanwhile, the trench-parallel pattern indicates some other possible causes of anisotropy. First, it may be due to the change in olivine LPO geometry that lead to the development of B-type olivine fabric where a low temperature, high stress, and high-water conditions exist in the mantle (Jung and Karato, 2001). Another plausible cause of trench-perpendicular pattern is shape preferred orientation (SPO) of partial melting since there is arc volcanism in the subduction system. The presence of partial melt can affect the olivine fabric geometry in the surrounding matrix, in addition to providing an SPO mechanism (Long, 2013).